Accepted Manuscript

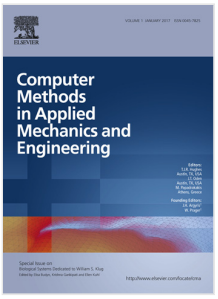

Identification of residual stresses in multi-layered arterial wall tissues using a variational framework

G.D. Ares, P.J. Blanco, S.A. Urquiza, R.A. Feijóo

PII: S0045-7825(16)30419-4
DOI: http://dx.doi.org/10.1016/j.cma.2017.02.028
Reference: CMA 11355

To appear in: *Comput. Methods Appl. Mech. Engrg.*

Received date: 23 May 2016
Revised date: 15 February 2017
Accepted date: 20 February 2017

Please cite this article as: G.D. Ares, P.J. Blanco, S.A. Urquiza, R.A. Feijóo, Identification of residual stresses in multi-layered arterial wall tissues using a variational framework, *Comput. Methods Appl. Mech. Engrg.* (2017), http://dx.doi.org/10.1016/j.cma.2017.02.028

Identification of residual stresses in multi-layered arterial wall tissues using a variational framework

G.D. Ares[a,c], P.J. Blanco[a,c], S.A. Urquiza[b,c], R.A. Feijóo[a,c]

[a] *National Laboratory for Scientific Computing, LNCC/MCTI, Av. Getúlio Vargas 333, Petrópolis, 25651-075, Brazil*
[b] *Department of Mechanical Engineering, Faculty of Engineering, National University of Mar del Plata, Av. J.B. Justo 4302, 7600, Mar del Plata, Argentina*
[c] *National Institute of Science and Technology in Medicine Assisted by Scientific Computing, INCT-MACC, Petrópolis, Brazil*

Abstract

In the past decades a considerable amount of literature has been published addressing the study of the mechanical behavior of arterial walls. Ex-vivo experimentation made possible the development of constitutive models and the characterization of material parameters contributing to the understanding of the mechanobiological response of vascular tissues. Moreover, the existence of residual stresses in configurations free of load was revealed, and its impact in the general stress state of the tissue was quantified. In recent years, data assimilation techniques have seen a rapid development in cardiovascular modeling field, primarily focusing on the estimation of material parameters for arterial wall segments using information provided by medical imaging as well as by in-vitro settings. However, concerning the estimation of residual stresses, this research field is in its early stages, and much work is still required for the full functional characterization of arterial tissues.

In this context, a conceptual variational framework for the development of residual stress estimation tools is proposed. Particularly, a variational formulation for the characterization of residual deformations and the associated stresses in arterial walls, based on full displacement field measurements of the vessel, is presented. Considering as known data the material parameters characterizing the behavior of the tissue and a set of arterial wall configurations at equilibrium with well defined pressure loads, we propose a cost functional that measures the mechanical imbalance caused by the lack of knowledge of residual stresses. In this manner, the characterization of residual stresses becomes a problem of minimizing such cost functional. Three numerical examples are presented highlighting the potential of the proposed approach. Among these examples, the characterization of residual stresses in a cylindrical geometry representing a three-layered aorta artery is performed.

Keywords: Residual deformations, residual stresses, arterial wall, characterization, variational formulation

1. Introduction

As it is well known, in order to realistically model and simulate the behavior of arterial tissues it is necessary to account for the different mechanical properties of arterial wall layers (intima, media, adventitia) considering the interaction of the structurally relevant components, namely: elastin, collagen fibers and smooth muscle cells [1]. A considerable amount of literature has been published addressing the study of the constitutive behavior of these soft tissues, developing comprehensive models [2, 3], and performing parameter estimation based on ex-vivo experimental data [4, 5]. However, it has also been recognized [2, 6, 7] that the in-vivo unloaded configuration of any vascular district is neither stress-free nor strain-free [8]. This led to an increasing number of investigations [9, 10] studying the effects of residual stresses (RSs) in arterial wall mechanics. In the last decades a shifting in the role researchers assign to RSs has taken place, from conceiving RSs as a mere side effect of growth to a conception in which RSs are viewed as an adaptive and protective mechanism. Certainly, residual strains and stresses have a functional role in determining suitable mechanobiological conditions in vascular vessels [11, 12]. In fact, arteries are living tissues that continuously adapt to their environment and to external stimuli [13, 14, 15]. This adaptation is mediated by growth and remodeling processes that lead to the occurrence of self-equilibrated RSs. In this connection, it has been pointed out [16] that RSs contribute to the transmural uniformity of the circumferential strains under physiological conditions, lowering stress gradients across the thickness of the vessel within each layer [17].

Reported experimental observations show that when an arterial segment is removed from its surroundings, RSs are manifested through the retraction of the vessel in the longitudinal direction as well as through the appearance of an opening angle when the wall is radially cut all along its axis. Moreover, in relatively recent works [5, 7], it has been observed that different levels of RSs are associated to the different constituent layers of the arterial wall. Most ef-

List of symbols	
Ω_v	Virtual (zero-stress) configuration
Ω_m	Material (zero-load) configuration
Ω_a, Ω_b^j	In-vivo configurations
Γ_m, Γ_a, Γ_b^j	Boundaries for configurations Ω_m, Ω_a, Ω_b^j
$\mathbf{x}_v$, $\mathbf{x}_m$, $\mathbf{x}_a$, $\mathbf{x}_b^j$	Coordinates associated to configurations Ω_v, Ω_m, Ω_a, Ω_b^j
$\mathbf{v}$, $\mathbf{w}^j$, $\mathbf{u}^j$	Displacement fields
$\mathbf{F}^r$	Residual deformation field
$\mathbf{F}^{\mathbf{v}}, \mathbf{F}^{\mathbf{w}}, \mathbf{F}^{\mathbf{u}}$	Deformation gradient tensors associated with $\mathbf{v}$, $\mathbf{w}^j$, $\mathbf{u}^j$
$\mathbf{F}^{\mathbf{v}r}, \mathbf{F}^{\mathbf{u}^j r}$	Total deformation gradient tensors for configurations Ω_a and Ω_b^j
N	Number of known configurations additional to Ω_a
p_a, p_b^j	Pressure levels applied in Ω_a and Ω_b^j
$\mathbf{S}^{(*)}$, $\mathbf{C}^{(*)}$	Second Piola-Kirchhoff and right Cauchy-Green tensors (superindex indicates related deformation)
$\boldsymbol{\sigma}^{(*)}$	Cauchy stress tensors (superindex indicates related deformation)
$\mathcal{V}$	Linear space of kinematically admissible variations
Kin_a	Linear manifold of kinematically admissible displacements defined in Ω_a
Ψ	Strain energy function
$\tilde{\mathbf{F}}^r$, $\tilde{\mathbf{v}}$	Arbitrary RRD and displacement fields
$\mathbf{F}^{\tilde{\mathbf{v}}}$ $\mathbf{F}^{\tilde{\mathbf{v}}\tilde{r}}, \mathbf{F}^{(\tilde{\mathbf{v}}+\mathbf{w}^j)\tilde{r}}$	Deformation tensors, considering arbitrary fields $\tilde{\mathbf{F}}^r$, $\tilde{\mathbf{v}}$
$\mathbf{D}$	Space of all tensor fields $\tilde{\mathbf{F}}_a^r$ defined in Ω_a with positive determinant
$\mathcal{R}_m$, $\mathcal{R}_{b,j}$	Functionals associated with the residuals of equilibrium equations
Φ_i	Elements of a basis for $\mathcal{V}_a$
R_m^i , $R_{b,j}^i$	Virtual power exerted between $\mathcal{R}_m$ and $\mathcal{R}_{b,j}$ and each element Φ_i
$\mathbf{R}_m$, $\mathbf{R}_b$	Vectors containing components R_m^i , $R_{b,j}^i$
η_m, η_b^j	Weighting parameters
$\mathcal{F}$, $\mathcal{J}$	Cost functionals
$(\cdot)_i$, $i = m, a$	Subindex denotes that the quantity is expressed in terms of coordinates $\mathbf{x}_i$
v, w	Displacement fields for 1D problems
e_σ, $e_{\mathbf{F}^r}$, e_v	Relative discrepancies for stress, deformation and displacement fields.

forts to account for RSs in arterial wall models are primarily based on the incorporation of prestrains that are usually determined through experimental procedures. These RSs are caused by the *recoverable residual deformations* [1] (RRDs) present in the tissue, and are necessary to maintain the kinematical compatibility at the structural level. Among these, we highlight the contributions of [1] with the first in-depth proposal of this idea, [5, 7] accounting for the different behaviors presented for each constituent layer, and [18, 19] displaying strategies to incorporate data obtained using experimental techniques into patient-specific geometries. It is also worthwhile to mention two different approaches explored in the literature, i) incorporating RSs through growth processes, considering that each mechanically relevant component is synthesized and deposited in the tissue with a predefined deformation (and consequently stress) level [20, 21]; and ii) introducing RSs to achieve a uniform transmural distribution of stresses in physiological conditions [22].

The past decade has seen a rapid development of data assimilation techniques in the field of cardiovascular modeling. Recent works have shown that, based on in-vivo data provided by medical images, these techniques can be used to estimate the in-vivo stress state of arterial segments in the presence of preloads [23, 24, 25], the unloaded configuration corresponding to those segments [8, 26, 27, 28, 29], or the material parameters characterizing the mechanical behavior of the soft tissues [30, 31, 32, 33, 34, 35, 36]. Remarkably, the predicted values for those material parameters are heavily influenced by the hypotheses considered to introduce the effect of residual stresses [37]. Despite these facts, the area of data assimilation in cardiovascular modeling is still in early stages of development and much work is yet to be done in order to develop effective tools to make the in-vivo estimation of RSs feasible.

In view of the gap highlighted in the previous paragraph, the aim of this work is to present a conceptual framework to aid the development of RS estimation tools. The proposed formulation consists in the definition of a cost functional which is able to measure the imbalance due to incorrect values of RRDs at a given set of equilibrated configurations of the arterial wall. Then, the characterization of RSs becomes an optimization problem where the residuals of the involved variational equations are minimized by finding the appropriate RRD field.

Fundamental to our purposes is to have at hand, as input data, the constitutive equation together with the corresponding material parameters characterizing the tissue behavior and at least two configurations of the arterial wall structure with the full displacement field between them. More generally, the proposed methodology is presented for an arbitrary number of known configurations. Three examples are featured for the verification of the proposed methodology. Furthermore, in these examples the influence of increasing amount of input data (in the form of known configurations) and the impact of errors in the material parameters is analyzed.

The structure of this article is organized as follows. The kinematic and mechanical setting for the RRD character-

[1] Recoverable in the sense that the energy stored in the material can be fully recovered when kinematic restrictions are released, for example, through excision of the tissue.

ization problem is presented in Section 2. The variational formulation of the problem and the proposed cost functional to be minimized are introduced in Section 3. A brief reference to the optimization techniques to be considered for our minimization problem is given in Section 4. Next, three numerical examples are presented to assess the capabilities of the proposed methodology in Section 5. Final remarks are outlined in Section 6.

2. Mechanical setting

As mentioned in the Section 1, the proposed approach relies in the fact that more than one arterial configuration is known. We will consider that $N+1$ configurations are known, say configuration Ω_a and configurations Ω_b^j, $j=1,\dots,N$, $N\geq 1$. For each one of these known configurations we also consider that the arterial blood pressure, which is the external load responsible for part of the total deformation occurring in these configurations, is given. Furthermore, the displacement vector field, say $\mathbf{w}^j$, which maps Ω_a into Ω_b^j are also considered as known data for all $j=1,\dots,N$.

2.1. Continuum mechanics basis

Consider the representative scheme displayed in Figure 1. The *virtual configuration* Ω_v (whose coordinates are denoted as $\mathbf{x}_v$) represents a state of unloaded and separated material constituents of the arterial wall, serving as a reference for the constitutive equations describing the material behavior. This virtual configuration has a zero stress state and is free of RRDs as result of removing all kinematical constraints and loads. Then, this configuration corresponds to a zero elastic strain energy configuration.

The material domain Ω_m (with coordinates $\mathbf{x}_m$) denotes a zero-load configuration. However, due to processes of growth and remodeling the material features a deformation, characterized in each material point by the RRD tensor $\mathbf{F}^r$ such that each infinitesimal fiber is related to its virtual counterpart by

$$d\mathbf{x}_m = \mathbf{F}^r d\mathbf{x}_v. \tag{1}$$

This RRD tensor is the recoverable part of the deformation of the tissue, and is responsible for storing energy in the structure even in the case of the zero-load configuration. The associated strain induces a self-equilibrated RS state, called $\boldsymbol{\sigma}^r$, that depends on the constitutive behavior of the material. For hyperelastic materials we admit the existence of a scalar strain energy function Ψ, from which the (second) Piola-Kirchhoff ($\mathbf{S}^r$) and Cauchy stress ($\boldsymbol{\sigma}^r$) tensors are obtained by

$$\mathbf{S}^r = \frac{\partial \Psi}{\partial \mathbf{C}^r}, \qquad \boldsymbol{\sigma}^r = \frac{1}{\det \mathbf{F}^r}\mathbf{F}^r\mathbf{S}^r\left(\mathbf{F}^r\right)^T, \tag{2}$$

where $\mathbf{F}^r$, $\boldsymbol{\sigma}^r$ and $\mathbf{S}^r$ are defined in terms of $\mathbf{x}_m$, and with $\mathbf{C}^r$ standing for the right Cauchy-Green deformation tensor given by $\mathbf{C}^r = \left(\mathbf{F}^r\right)^T\mathbf{F}^r$.

The spatial domains Ω_a and Ω_b^j (with $j=1,\dots,N$ and coordinates respectively denoted as $\mathbf{x}_a$ and $\mathbf{x}_b^j$) are configurations at equilibrium with different levels of blood pressure, say p_a and p_b^j which are applied over the inner surface of the vessel, Γ_a and Γ_b^j, respectively. Coordinates in each domain are related through the displacement fields $\mathbf{v}$ and $\mathbf{u}^j$ as follows [2]

$$\mathbf{x}_a = \mathbf{x}_m + \mathbf{v}_m, \tag{3}$$

$$\mathbf{x}_b^j = \mathbf{x}_m + \mathbf{u}_m^j. \tag{4}$$

In addition, the relation between configurations Ω_a and Ω_b^j can be stated in terms of the N displacement fields $\mathbf{w}^j$, as next

$$\mathbf{x}_b^j = \mathbf{x}_a + \mathbf{w}_a^j. \tag{5}$$

Hence, the deformation gradient tensors are obtained as follows

$$\begin{aligned}\mathbf{F}^{\mathbf{u}^j} &= \mathbf{I} + \nabla_m \mathbf{u}_m^j,\\ \mathbf{F}^{\mathbf{v}} &= \mathbf{I} + \nabla_m \mathbf{v}_m,\\ \mathbf{F}^{\mathbf{w}^j} &= \mathbf{I} + \nabla_a \mathbf{w}_a^j.\end{aligned} \tag{6}$$

where $\mathbf{F}^{\mathbf{u}^j}$ and $\mathbf{F}^{\mathbf{v}}$ are defined in terms of $\mathbf{x}_m$, $\mathbf{F}^{\mathbf{w}^j}$ in terms of $\mathbf{x}_a$ and $\mathbf{F}^{\mathbf{v}r}$, $\mathbf{F}^{\mathbf{u}^j r}$ (see (8) below) and $\mathbf{F}^r$ in terms of $\mathbf{x}_m$. Also, note that the deformation gradient tensors, $\mathbf{F}^{\mathbf{v}}$ and $\mathbf{F}^{\mathbf{u}^j}$, are related through

$$\mathbf{F}^{\mathbf{u}^j} = \mathbf{F}_m^{\mathbf{w}^j}\mathbf{F}^{\mathbf{v}}, \tag{7}$$

where subindex m indicates that $\mathbf{F}_m^{\mathbf{w}^j}$ is expressed in terms of $\mathbf{x}_m$. The total deformation experienced by the material at these configurations is obtained composing the presented deformation gradient tensors with $\mathbf{F}^r$, obtaining

$$\mathbf{F}^{\mathbf{u}^j r} = \mathbf{F}^{\mathbf{u}^j}\mathbf{F}^r = \mathbf{F}_m^{\mathbf{w}^j}\mathbf{F}^{\mathbf{v}}\mathbf{F}^r, \qquad \mathbf{F}^{\mathbf{v}r} = \mathbf{F}^{\mathbf{v}}\mathbf{F}^r. \tag{8}$$

Therefore, the corresponding right Cauchy-Green deformation tensors are

$$\mathbf{C}^{\mathbf{v}r} = (\mathbf{F}^{\mathbf{v}r})^T\mathbf{F}^{\mathbf{v}r}, \qquad \mathbf{C}^{\mathbf{u}^j r} = (\mathbf{F}^{\mathbf{u}^j r})^T\mathbf{F}^{\mathbf{u}^j r}, \tag{9}$$

which are naturally defined in Ω_m.

2.2. Mechanical equilibrium

In this section the formulations corresponding to the mechanical equilibrium of the tissue in configurations Ω_m, Ω_a and Ω_b^j are introduced. Moreover, these equations will be conveniently rewritten in configuration Ω_a.

[2] Hereafter, indexes m, a, b denote a dependency with respect to coordinates $\mathbf{x}_m$, $\mathbf{x}_a$ and $\mathbf{x}_b^j$, respectively

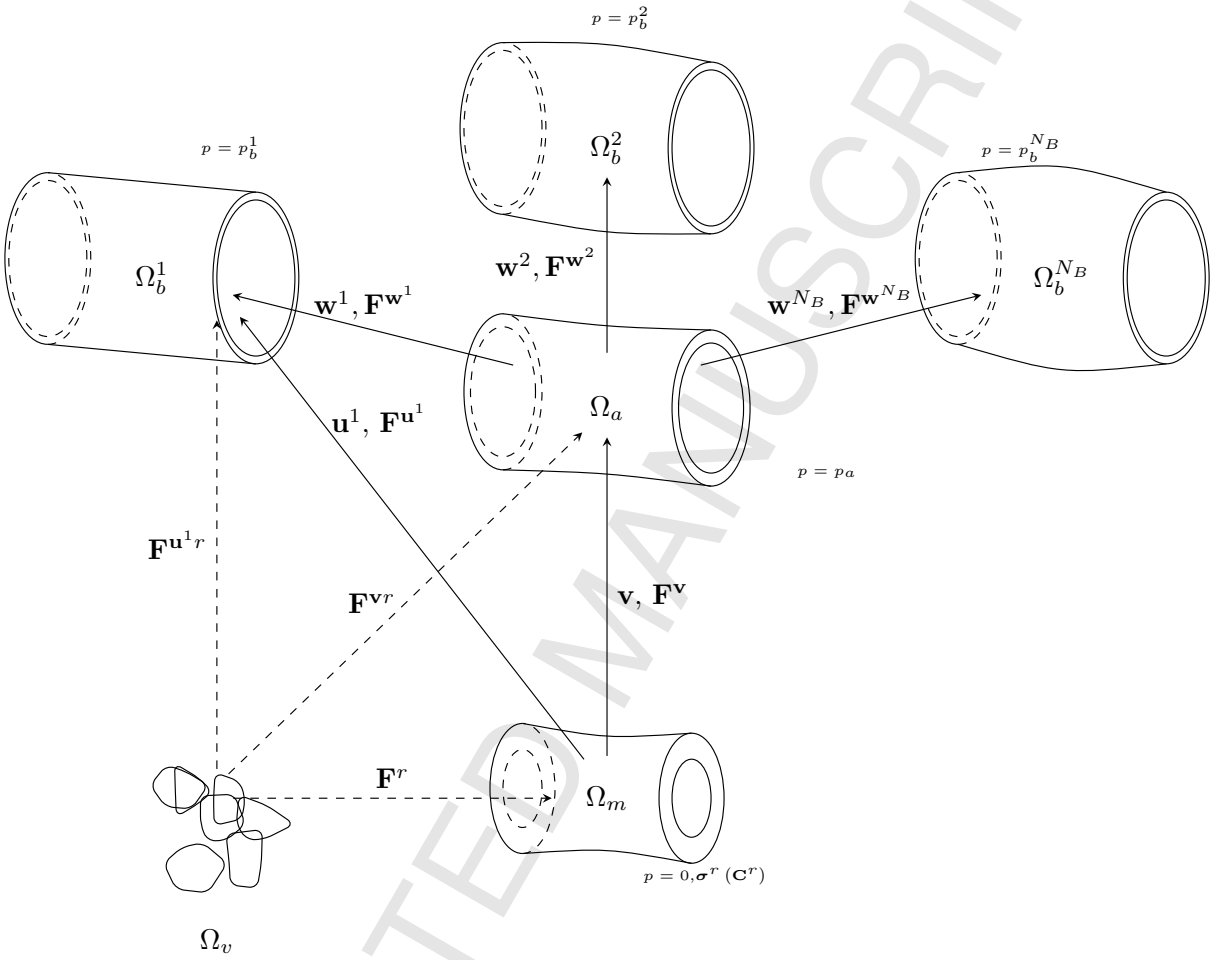

Figure 1: Problem setting for residual deformation characterization. The virtual configuration Ω_v represents a disaggregated state of material particles composing the arterial wall in a zero-stress state and serves as reference configuration for constitutive equations (no elastic energy is stored). The material domain Ω_m is subjected to no external loads, however, due to the existence of RRDs ($\mathbf{F}^r$) developed during the processes of growth/remodeling, a self-equilibrated residual stress state ($\boldsymbol{\sigma}^r$) arises in this configuration. Configuration Ω_a and the N configurations Ω_b^j ($j = 1, \ldots, N$) represent equilibrium domains with their corresponding external loading system given by the arterial blood pressure (p_a and p_b^j, respectively). These N configurations are represented in the figure by Ω_b^1, Ω_b^2 and Ω_b^N. Tensors $\mathbf{F}^{\mathbf{v}}$ and $\mathbf{F}^{\mathbf{u}^j}$ (only $\mathbf{F}^{\mathbf{u}^1}$ is shown for the sake of clarity) denote the corresponding deformation gradient tensors due to the aforementioned displacement fields, and $\mathbf{F}^{\mathbf{v}r} = \mathbf{F}^{\mathbf{v}}\mathbf{F}^r$, $\mathbf{F}^{\mathbf{u}^j r} = \mathbf{F}^{\mathbf{u}^j}\mathbf{F}^r$ (only $\mathbf{F}^{\mathbf{u}^1 r}$ is shown for the sake of clarity) are the material expressions for the total deformation tensor with respect to the constitutive reference configuration Ω_v (virtual configuration). For the purposes of the present work, Ω_v will never be practically used, Ω_m is unknown in the problem, while Ω_a and Ω_b^j are known data, as well as displacement fields $\mathbf{w}^j$.

2.2.1. Material configuration Ω_m

The variational equation that defines the mechanical equilibrium of the body in Ω_m reads

$$\int_{\Omega_m} \boldsymbol{\sigma}^r \cdot \nabla_m^s \hat{\mathbf{v}}\, d\Omega_m = 0 \qquad \forall \hat{\mathbf{v}} \in \mathcal{V}_m, \tag{10}$$

where $\boldsymbol{\sigma}^r$ is a RS field, ∇_m^s denotes the symmetric gradient with respect to coordinates $\mathbf{x}_m$, and $\mathcal{V}_m$ is the linear space of kinematically admissible variations in the material configuration considering the Dirichlet boundary Γ_m^D, which is given by

$$\mathcal{V}_m = \left\{ \mathbf{u} \in \mathbf{H}^1(\Omega_m)\,;\ \mathbf{u}|_{\Gamma_m^D} = 0 \right\}, \tag{11}$$

where $\mathbf{H}^1(\Omega_m)$ denotes the Hilbert space of functions, with square-integrable gradient, defined in Ω_m. Since in the characterization problem Ω_m is unknown, it is worthwhile to express equation (10) in terms of $\mathbf{x}_a$, allowing to perform the integration in the known configuration Ω_a. A change of variables leads to

$$\int_{\Omega_a} \boldsymbol{\sigma}_a^r \cdot ((\mathbf{F}_a^{\mathbf{v}})^{-T} \nabla_a \hat{\mathbf{v}})^s\, d\Omega_a = 0 \quad \forall \hat{\mathbf{v}} \in \mathcal{V}_a, \tag{12}$$

where $\mathcal{V}_a$ is the counterpart of $\mathcal{V}_m$ in Ω_a, and $\boldsymbol{\sigma}_a^r$ is related to $\boldsymbol{\sigma}^r$ and $\mathbf{S}^r$ through the following expressions

$$\begin{aligned} \boldsymbol{\sigma}_a^r &= \frac{1}{\det \mathbf{F}_a^{\mathbf{v}}} \mathbf{F}_a^{\mathbf{v}} (\boldsymbol{\sigma}^r)_a (\mathbf{F}_a^{\mathbf{v}})^T \\ &= \frac{1}{\det \mathbf{F}_a^{\mathbf{v}r}} \mathbf{F}_a^{\mathbf{v}r} (\mathbf{S}^r)_a (\mathbf{F}_a^{\mathbf{v}r})^T . \end{aligned} \tag{13}$$

2.2.2. Spatial configuration Ω_a

For the sake of simplicity, let us consider that the arterial wall is only subjected to a pressure load p_a applied on the inner surface of the vessel Γ_a (the extension to more general load cases is straightforward). Then, the variational equation that characterizes the mechanical equilibrium for the spatial configuration Ω_a reads

$$\begin{aligned} \int_{\Omega_a} \boldsymbol{\sigma}^{\mathbf{v}r} \cdot \nabla_a^s \hat{\mathbf{v}}\, d\Omega_a = \\ \int_{\Gamma_a} p_a \mathbf{n}_a \cdot \hat{\mathbf{v}}\, d\Gamma_a \qquad \forall \hat{\mathbf{v}} \in \mathcal{V}_a, \end{aligned} \tag{14}$$

where $\mathcal{V}_a$ is the space of kinematically admissible virtual actions in Ω_a, and $\boldsymbol{\sigma}^{\mathbf{v}r}$ is

$$\boldsymbol{\sigma}^{\mathbf{v}r} = \frac{1}{\det \mathbf{F}_a^{\mathbf{v}r}} \mathbf{F}_a^{\mathbf{v}r} (\mathbf{S}^{\mathbf{v}r})_a (\mathbf{F}_a^{\mathbf{v}r})^T , \tag{15}$$

with $\mathbf{S}^{\mathbf{v}r}$ the second Piola-Kirchhoff stress tensor related to the deformation $\mathbf{F}^{\mathbf{v}r}$.

2.2.3. Spatial configurations Ω_b^j

Analogously to the previous case, for each configuration Ω_b^j $(j = 1, \ldots, N)$ with a given pressure p_b^j applied over the inner surface of the vessel wall Γ_b^j, the variational equations characterizing the mechanical equilibriums reads

$$\begin{aligned} \int_{\Omega_b^j} \boldsymbol{\sigma}^{\mathbf{u}^j r} \cdot \nabla_b^s \hat{\mathbf{v}}\, d\Omega_b^j = \int_{\Gamma_b^j} p_b^j \mathbf{n}_b \cdot \hat{\mathbf{v}}\, d\Gamma_b^j \qquad \forall \hat{\mathbf{v}} \in \mathcal{V}_b^j, \\ j = 1, \ldots, N, \end{aligned} \tag{16}$$

where $\mathcal{V}_b^j$ is the space of kinematically admissible virtual actions in Ω_b^j, and the constitutive stress tensors $\boldsymbol{\sigma}^{\mathbf{u}^j r}$ are obtained through

$$\boldsymbol{\sigma}^{\mathbf{u}^j r} = \frac{1}{\det \mathbf{F}_b^{\mathbf{u}^j r}} \mathbf{F}_b^{\mathbf{u}^j r} (\mathbf{S}^{\mathbf{u}^j r})_b (\mathbf{F}_b^{\mathbf{u}^j r})^T , \tag{17}$$

where $\mathbf{F}^{\mathbf{u}^j r}$ and $\mathbf{S}^{\mathbf{u}^j r}$ are the deformation and second Piola-Kirchhoff stress tensors associated with the displacements $\mathbf{u}^j = \mathbf{w}^j + \mathbf{v}$. Furthermore, since $\mathbf{w}^j$ is given data, we can reduce the number of unknown variables. In fact, $\mathbf{u}^j$ can be eliminated considering the identities $\mathbf{u}^j = \mathbf{v} + \mathbf{w}^j$ and $\mathbf{F}_a^{\mathbf{u}^j r} = \mathbf{F}_a^{(\mathbf{v}+\mathbf{w}^j)r} = \mathbf{F}^{\mathbf{w}^j} \mathbf{F}_a^{\mathbf{v}} \mathbf{F}_a^r$.

Then, these variational equations expressed in terms of $\mathbf{x}_a$ coordinates read

$$\begin{aligned} \int_{\Omega_a} \boldsymbol{\sigma}_a^{(\mathbf{v}+\mathbf{w}^j)r} \cdot ((\mathbf{F}^{\mathbf{w}^j})^T \nabla_a \hat{\mathbf{v}})^s\, d\Omega_a = \\ \int_{\Gamma_a} (p_b^j)_a (\mathbf{F}^{\mathbf{w}^j})^{-T} \mathbf{n}_a \cdot \hat{\mathbf{v}} \det \mathbf{F}^{\mathbf{w}^j}\, d\Gamma_a \qquad \forall \hat{\mathbf{v}} \in \mathcal{V}_a, \\ j = 1, \ldots, N. \end{aligned} \tag{18}$$

where $\boldsymbol{\sigma}_a^{\mathbf{u}^j r} = \boldsymbol{\sigma}_a^{(\mathbf{v}+\mathbf{w}^j)r}$ is written as

$$\boldsymbol{\sigma}_a^{(\mathbf{v}+\mathbf{w}^j)r} = \frac{1}{\det \mathbf{F}_a^{\mathbf{v}r}} \mathbf{F}_a^{\mathbf{v}r} (\mathbf{S}^{(\mathbf{v}+\mathbf{w}^j)r})_a (\mathbf{F}_a^{\mathbf{v}r})^T . \tag{19}$$

3. Recoverable residual deformation characterization problem

In this Section, the RRD identification problem is introduced as the minimization of a cost functional measuring the mechanical disequilibrium of the setting described above caused by an inconsistent RRD field.

We consider that domains Ω_a and Ω_b^j $(j = 1, \ldots, N)$, each one in equilibrium with known pressure fields p_a and p_b^j, together with the displacements vectors fields $\mathbf{w}^j$ are given data. Hence, the objective is to find the RRD field $\mathbf{F}^r$ (from which the RS field $\boldsymbol{\sigma}^r$ directly follows) and the material configuration Ω_m (and consequently the displacement fields $\mathbf{u}^j$ and $\mathbf{v}$), such that the $(N+2)$ mechanical problems stated by (12), (14) and (18) are satisfied.

Let now $(\mathbf{F}^r, \mathbf{v})$ be the solution of equations (12), (14) and (18) (observe that if the pair is solution of (12) and (14), then equations (18) are satisfied). In the following, consider an arbitrary displacement $\tilde{\mathbf{v}} \neq \mathbf{v}$, and an arbitrary deformation tensor $\tilde{\mathbf{F}}^r \neq \mathbf{F}^r$. $\tilde{\mathbf{v}}$ is defined in configuration Ω_a. Also, note that $\tilde{\mathbf{v}} \in \mathrm{Kin}_a$, where Kin_a

stands for the linear manifold of kinematically admissible displacements defined in Ω_a and is given by

$$\text{Kin}_a = \left\{ \mathbf{u} \in \mathbf{H}^1(\Omega_a);\ \mathbf{u}|_{\Gamma_a^D} = \overline{\mathbf{v}} \right\}. \tag{20}$$

As the pair $(\tilde{\mathbf{F}}_a^r, \tilde{\mathbf{v}})$ is not solution of the problem, for a fixed pair, the following functionals can be defined in $\mathcal{V}_a'$:

- $\mathcal{R}_m = \mathcal{R}_m(\tilde{\mathbf{F}}_a^r, \tilde{\mathbf{v}}) \in \mathcal{V}_a'$, associated with the mechanical disequilibrium of the RS field $\boldsymbol{\sigma}^r$ in Ω_m; i.e., with the residual of equation (12), that is

$$\langle \mathcal{R}_m(\tilde{\mathbf{F}}_a^r, \tilde{\mathbf{v}}), \hat{\mathbf{v}} \rangle = \int_{\Omega_a} \boldsymbol{\sigma}_a^{\tilde{r}} \cdot ((\mathbf{F}_a^{\tilde{\mathbf{v}}})^{-T} \nabla_a \hat{\mathbf{v}})^s \, d\Omega_a \quad \hat{\mathbf{v}} \in \mathcal{V}_a, \tag{21}$$

  where $\boldsymbol{\sigma}_a^{\tilde{r}}$ is the residual stress related to $\tilde{\mathbf{F}}_a^r$ and the notation $\langle a, b \rangle$ indicates an inner product between the elementss $a \in \mathcal{V}_a$ and an element b defined in its dual space ($b \in \mathcal{V}_a'$). Observe that this functional depends explicitly and implicitly (through $\boldsymbol{\sigma}_a^{\tilde{r}}$) on $\tilde{\mathbf{F}}_a^r$.

- The N functionals $\mathcal{R}_{b,j} = \mathcal{R}_{b,j}(\tilde{\mathbf{F}}_a^r, \tilde{\mathbf{v}}) \in \mathcal{V}_a'$, associated with the mechanical disequilibrium in the known spatial domain Ω_b^j given by the residuals of equations (18). They are defined by

$$\langle \mathcal{R}_{b,j}(\tilde{\mathbf{F}}_a^r, \tilde{\mathbf{v}}), \hat{\mathbf{v}} \rangle = \int_{\Omega_a} \boldsymbol{\sigma}_a^{(\tilde{\mathbf{v}}+\mathbf{w}^j)\tilde{r}} \cdot ((\mathbf{F}^{\mathbf{w}^j})^T \nabla_a \hat{\mathbf{v}})^s \, d\Omega_a - \int_{\Gamma_a} (p_b^j)_a (\mathbf{F}^{\mathbf{w}^j})^{-T} \mathbf{n}_a \cdot \hat{\mathbf{v}} \det \mathbf{F}^{\mathbf{w}^j} \, d\Gamma_a, \quad \hat{\mathbf{v}} \in \mathcal{V}_a, \quad i = 1, \ldots, N, \tag{22}$$

  where $\boldsymbol{\sigma}_a^{(\tilde{\mathbf{v}}+\mathbf{w}^j)\tilde{r}}$ denotes the Cauchy stress associated to the deformation $\mathbf{F}^{(\tilde{\mathbf{v}}+\mathbf{w}^j)\tilde{r}}$ expressed in terms of $\mathbf{x}_a$. Again, note that this functional depends explicitly and implicitly (through $\boldsymbol{\sigma}_a^{(\tilde{\mathbf{v}}+\mathbf{w}^j)\tilde{r}}$) on $\tilde{\mathbf{F}}_a^r$.

Furthermore, let $\mathcal{V}_a = span\{\Phi_1, \Phi_2, \ldots\}$, where Φ_i denotes the i-th element of that basis. Then, the above functionals are completely characterized through the defined inner products with each element Φ_i of the proposed basis, i.e., by the virtual power exerted between the generalized residual forces $\mathcal{R}_m$ and $\mathcal{R}_{b,j}$ and each element of the basis.

$$R_m^i(\tilde{\mathbf{F}}_a^r, \tilde{\mathbf{v}}) = \langle \mathcal{R}_m(\tilde{\mathbf{F}}_a^r, \tilde{\mathbf{v}}), \Phi_i \rangle, \quad i = 1, 2, \ldots \tag{23}$$

$$R_{b,j}^i(\tilde{\mathbf{F}}_a^r, \tilde{\mathbf{v}}) = \langle \mathcal{R}_{b,j}(\tilde{\mathbf{F}}_a^r, \tilde{\mathbf{v}}), \Phi_i \rangle, \quad i = 1, 2, \ldots \quad j = 1, \ldots, N \tag{24}$$

Moreover, if $(\mathbf{F}^r, \mathbf{v})$ is the solution of equations (12), (14) and the set of N equations defined by (18) then, such pair makes $R_m^i = R_{b,j}^i = 0$ $i = 1, , 2, \ldots,$ $j = 1, \ldots, N$. Then, we introduce the following *cost functional* that characterizes the mechanical imbalance as a function of the RRDs

$$\mathcal{J}(\tilde{\mathbf{F}}_a^r, \tilde{\mathbf{v}}) = \frac{\eta_m}{2} \mathbf{R}_m(\tilde{\mathbf{F}}_a^r, \tilde{\mathbf{v}}) \cdot \mathbf{R}_m(\tilde{\mathbf{F}}_a^r, \tilde{\mathbf{v}}) + \sum_{j=1}^{N} \frac{\eta_b^j}{2} \mathbf{R}_{b,j}(\tilde{\mathbf{F}}_a^r, \tilde{\mathbf{v}}) \cdot \mathbf{R}_{b,j}(\tilde{\mathbf{F}}_a^r, \tilde{\mathbf{v}}), \tag{25}$$

where $\mathbf{R}_m$ and $\mathbf{R}_b$ are vectors containing the components defined in (23) and (24), respectively. Also, η_m and η_b^j are weighting factors corresponding to the mechanical imbalances at Ω_m and Ω_b^j, respectively.

Given a fixed $\tilde{\mathbf{F}}_a^r$, consider now $\check{\mathbf{v}} = \check{\mathbf{v}}(\tilde{\mathbf{F}}_a^r)$ the solution of equation (14). Then, the RRD identification problem can be written in the following variational form: given Ω_a, the N configurations Ω_b^j, the N displacements fields $\mathbf{w}^j$, the corresponding inner pressure fields p_a, p_b^j and the material parameters characterizing the arterial wall constitutive behavior, find $\mathbf{F}_a^r$ such that

$$\mathbf{F}_a^r := \arg\min_{\mathbf{D}} \left\{ \mathcal{J}(\tilde{\mathbf{F}}_a^r, \check{\mathbf{v}}(\tilde{\mathbf{F}}_a^r)) \right\},$$

where $\check{\mathbf{v}}(\tilde{\mathbf{F}}_a^r)$ stands for the relation given by

$$\int_{\Omega_a} \boldsymbol{\sigma}^{\check{\mathbf{v}}\tilde{r}} \cdot \nabla_a^s \hat{\mathbf{v}} \, d\Omega_a - \int_{\Gamma_a} p_a \mathbf{n}_a \cdot \hat{\mathbf{v}} \, d\Gamma_a = 0 \quad \forall \hat{\mathbf{v}} \in \mathcal{V}_a. \tag{26}$$

In the problem described above, $\arg\min\{\mathcal{J}\}$ stands for the argument that minimizes the functional $\mathcal{J}$ and $\mathbf{D}$ indicates the space of all tensor fields $\tilde{\mathbf{F}}_a^r$ associated with RRDs defined in Ω_a with positive determinant (i.e. $\det \tilde{\mathbf{F}}_a^r > 0$) for any $\mathbf{x}_a \in \Omega_a$. Additionally, we recall that $\boldsymbol{\sigma}^{\check{\mathbf{v}}r}$ is defined as

$$\boldsymbol{\sigma}^{\check{\mathbf{v}}r} = \frac{1}{\det \mathbf{F}_a^{\check{\mathbf{v}}r}} \mathbf{F}_a^{\check{\mathbf{v}}r} \left(\mathbf{S}^{\check{\mathbf{v}}r} \right)_a \left(\mathbf{F}_a^{\check{\mathbf{v}}r} \right)^T. \tag{27}$$

As $\mathcal{J}(\tilde{\mathbf{F}}_a^r, \check{\mathbf{v}}(\tilde{\mathbf{F}}_a^r)) \geq 0 \quad \forall \tilde{\mathbf{F}}_a^r \in \mathbf{D}$ this problem is well defined, and $\mathcal{J}(\mathbf{F}_a^r, , \check{\mathbf{v}}(\tilde{\mathbf{F}}_a^r)) = 0$ is obtained if $(\mathbf{F}_a^r, \check{\mathbf{v}}(\mathbf{F}_a^r)) \in \mathbf{D} \times \text{Kin}_a$ satisfies the mechanical equilibrium equations for Ω_m, Ω_a and Ω_b^j -given by (12), (14) and (18), respectively.

Remark 1. *For the problems under study in this work, we do not have at hand an explicit form for cost functional $\mathcal{J}$ as a function of the residual deformations $\tilde{\mathbf{F}}_a^r$. In fact, in the optimization problem to be applied we just need to evaluate the cost functional $\mathcal{J}$ at a given point. This evaluation is a two step process. First, given Ω_a and $\tilde{\mathbf{F}}_a^r$, the mechanical equilibrium given by equation (14) is evaluated, yielding $\check{\mathbf{v}}(\tilde{\mathbf{F}}_a^r)$. Note that this nonlinear problem requires a linearization procedure. Here we employ a Newton method as described in the supplementary material. Next, given $\check{\mathbf{v}}(\tilde{\mathbf{F}}_a^r)$ we compute $\mathcal{J}(\tilde{\mathbf{F}}_a^r, \check{\mathbf{v}}(\tilde{\mathbf{F}}_a^r))$ through the evaluation of the residuals in the equilibrium equations related to configurations Ω_m and Ω_b^j. This amounts to*

compute the duality products given by equations (23) *and* (24)*, respectively, which are explicitly given by expressions* (21) *and* (22) *correspondingly.*

4. Optimization methods

The RRD characterization problem is completely defined by problem (26), hence leading to a minimization of a nonlinear functional subjected to an also nonlinear equality constraint. In order to perform this minimization, two methods are explored in the numerical examples (see Section 5), for the first numerical example (see Section 5.1) a simple gradient method is used and, for the second and third examples (Sections 5.2 and 5.3) we make use of an interior-point algorithm for constrained optimization available in the MATLAB® Optimization Toolbox™ [38], based on the works of Byrd reported in [39, 40].

5. Numerical examples

In this section three numerical examples are presented to assess the potentiality of the mechanical setting for the characterization of RRDs in arterial tissues.

In all the examples, from a proposed material configuration and its corresponding residual deformation field, a complete solution (including the equilibrium configurations Ω_a, Ω_b^j, their corresponding load states and displacement fields $\mathbf{w}^j$) will be manufactured to verify the proposed methodology. Numerical implementation for the mechanical equilibrium problem (utilized in the manufacturing of the known setting) and the evaluation of the residuals involved in the cost functional were developed using MATLAB®[38].

5.1. Clamped bar

5.1.1. Problem description

In this example, a one-dimensional bar clamped at both ends is considered where the material configuration, Ω_m, occupies the interval $[0, 2L]$. A load f, distributed in the cross-sectional area of the bar, is applied at the material point P located in the center of Ω_m, i.e. at $x_m = L$. A representative scheme of the problem is presented in Figure 2. The constitutive behavior of the material is characterized by a linear relation between the second Piola-Kirchhoff stress and the deformation tensor, i.e.

$$S = k_b(F - 1), \tag{28}$$

where k_b represents an elastic parameter and $F = F^v F^r$ is the total deformation gradient resulting from the composition between a deformation field due to the displacement v and the RRDs F^r. In particular, a constant field F^r is admitted for the material configuration Ω_m. Consequently, through (28), S^r is also a constant field.

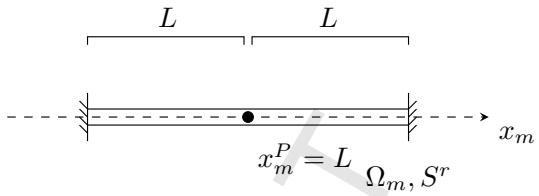

Figure 2: Setting for the clamped bar 1D problem

When the concentrated load f is applied, the analytical solution for the equilibrium problem can be easily obtained, resulting in a piecewise linear displacement field v_m, which presents null values at both ends and maximum at the point $x_m = L$, i.e.

$$v_m(x_m) = \begin{cases} \frac{f}{2(k_b F^r + S^r)F^r} x_m, & x_m \in [0, L], \\ \frac{f}{2(k_b F^r + S^r)F^r} (2L - x_m), & x_m \in [L, 2L]. \end{cases} \tag{29}$$

We introduce the notation $v^f = v(x_m)$ to emphasize the fact that this displacement field is associated to the load f.

From the above displacement field, the equilibrium configuration $\Omega_f = [0, 2L]$ is defined. Observe that despite the fact that Ω_m and Ω_f occupy the same region in the Euclidean space, points in $[0, 2L]$ correspond to different material points depending which configuration is considered. Furthermore, the solution of the problem belongs to the space spanned by linear finite elements shape functions, provided a node is placed at the point $x_m = L$.

5.1.2. Manufactured solution: data and target

The geometry and constitutive behavior are defined by $L = 1$ m, $k_b = 1.0 \cdot 10^3$ Pa. The value characterizing the constant RRD field is set as $F^r = 1.01$, defining the objective for the identification problem. Note that, from (28), the constant RS field is given by $S^r = 10$ Pa.

Let us now consider that two equilibrium configurations, Ω_a and Ω_b, are known ($N = 1$). $\Omega_a = [0, 2L]$ is at equilibrium with the concentrated load $f_a = 100$ Pa. Then, using (29), we obtain the load application point for the force f_a as $x_a^{f_a} = L + v^{f_a} = 1.0485$ m. Similarly, $\Omega_b = [0, 2L]$ is at equilibrium with $f_b = 200$ Pa, applied at $x_b^{f_b} = L + v^{f_b} = 1.0970$ m.

Finally, the displacement field w, mapping points from Ω_a into Ω_b is given by

$$w(x_a) = \begin{cases} 0.0485 \text{ m} \frac{x_a}{1.0485 \text{ m}}, & x_a \in [0 \text{ m}, 1.0485 \text{ m}], \\ 0.0485 \text{ m} \frac{x_a - 2L}{1.0485 \text{ m} - 2L}, & x_a \in [1.0485 \text{ m}, 2L]. \end{cases} \tag{30}$$

Summarizing, the data for the identification problem is given by: the constitutive equation (28), the constitutive parameter k_b, $\Omega_a = [0, 2L]$, f_a (with its application point $x_a^{f_a}$), $\Omega_b = [0, 2L]$, f_b (with its application point $x_b^{f_b}$). Note that, through $x_a^{f_a}$ and $x_b^{f_a}$ the value of the displacement field w at the load application point is also provided. Additionally, the target RRD field for the identification prob-

lem is the constant field $F^r = 1.01$. As consequence, the associated fields S^r, $v = v^{f_a}$ and $u = v^{f_b}$ are also defined as targets.

5.1.3. Optimization problem

For the numerical approximation we employ linear finite elements for the displacement field and for the Lagrange multiplier (involved in computation of the functional sensitivity, as can be observed in the supplementary material). The spatial discretization is performed in the Ω_a configuration using only two finite elements, considering three nodes: two located at both ends (constrained due to the boundary conditions), and one at the load application point P.

Additionally, a constant RRD field $\tilde{F}^r_{a,e}$ $(e = 1, 2)$ within each element is considered and the cost functional is minimized using a simple gradient descent method. At each optimization iteration k, the current guess for the residual deformation field $\tilde{F}^r_{a,e}$ is updated through

$$(\tilde{F}^r_{a,e})^{k+1} = (\tilde{F}^r_{a,e})^k - \Delta F^e, \tag{31}$$

where superscript k indicates the k-th iteration of the minimization process and ΔF^e is defined as

$$\Delta F^e = \gamma \left\langle \frac{\partial \mathcal{J}}{\partial \tilde{F}^r_a}, \delta \tilde{F}^r_{a,e} \right\rangle \Big|_{(\tilde{F}^r_a)^k}, \tag{32}$$

if $|\gamma \left\langle \frac{\partial \mathcal{J}}{\partial \tilde{F}^r_a}, \delta \tilde{F}^r_{a,e} \right\rangle \Big|_{(\tilde{F}^r_a)^k}| < \Delta^M$, or

$$\Delta F^e = sign \left(\left\langle \frac{\partial \mathcal{J}}{\partial \tilde{F}^r_a}, \delta \tilde{F}^r_{a,e} \right\rangle \Big|_{(\tilde{F}^r_a)^k} \right) \Delta^M \tag{33}$$

otherwise. In these expressions, $(\tilde{F}^r_a)^k$ indicates the set of elemental values $\tilde{F}^r_{a,e}$ at iteration k. The process is stopped when the convergence criterion $\mathcal{J}(\tilde{F}^r_a) < tol^j$ is met. The parameters controlling the optimization process are defined as $\Delta^M = 10^{-2}$, $\gamma = 10^{-7}$ and $tol^j = 10^{-3}$. Also, the weighting factors have been set to $\eta_m = 1$ and $\eta_b = 100$. This choice is made considering that with the proposed initial condition any material configuration will be at equilibrium, and, as consequence, at such point the algorithm should be mainly driven by the mechanical imbalance occurring in Ω_b configuration.

The initial guess is set as $\tilde{F}^r_a|_{\Omega_a} = 1$ and the functional gradient $\left\langle \frac{\partial \mathcal{J}}{\partial \tilde{F}^r_a}, \delta \tilde{F}^r_{a,e} \right\rangle \Big|_{(\tilde{F}^r_a)^k}$ is computed through the sensitivity analysis available in the supplementary material.

5.1.4. Results

Figure 3 summarizes the results. In Figure 3(a), the behavior of the descending algorithm through the minimization of the cost functional is shown. In Figure 3(b) it is clearly observed that the material configuration is recovered when convergence is achieved. Finally, Figure 3(c) displays the convergence of the RRD values for both finite elements.

5.1.5. Discussion

In this first example, a verification of the variational framework in a simple problem where the exact solution is known is performed. Using a standard gradient descent method the viability and potential of the proposed mechanical setting for the estimation of RRDs (and the corresponding RSs) along with the zero-load (material) configuration have been shown.

5.2. Thick-walled cylinder

5.2.1. Problem description

In this example the identification of RRDs is performed in an homogeneous thick-walled cylinder subjected to uniform internal pressure. Considering such conditions, the problem possess rotational symmetry. As in the previous example, a complete setting will be manufactured from a known material configuration at equilibrium with a known RS field (originated by predefined RRDs). Then, based on the manufactured data set, the proposed method will be utilized to identify the RRD field.

In this context, it is useful to introduce the kinematic setting corresponding to this case with rotational symmetry. Consider a cylindrical material configuration, with points defined by

$$\mathbf{x}_m = (\rho_m, \theta_m, z_m), \tag{34}$$

where as usual, ρ_m denotes the radial coordinate, θ_m the angular coordinate, and z_m the axial coordinate. Considering the rotational symmetry, shear stresses and the tangential component of the displacement field are null. Moreover, we also consider a pipe of fixed length and constant strains in the axial direction. Thence, the space of kinematically admissible displacements $\mathcal{U}_m$ and the space of associated kinematically admissible variations $\mathcal{V}_m$ are given by

$$\mathcal{V}_m = \mathcal{U}_m = \{\mathbf{u} = (u^\rho, 0, 0) \mid u^\rho \in \mathcal{U}^\rho_m\}, \tag{35}$$

with

$$\mathcal{U}^\rho_m = \left\{ u^\rho \in H^1(\Omega_m) \mid \frac{\partial u^\rho}{\partial \theta_m}\Big|_{\Omega_m} = \frac{\partial u^\rho}{\partial z_m}\Big|_{\Omega_m} = 0 \right\}. \tag{36}$$

And, for an element $\mathbf{u} \in \mathcal{U}_m$ its gradient takes the following form

$$\nabla_m \mathbf{u} = \begin{bmatrix} \frac{\partial u^\rho}{\partial \rho_m} & 0 & 0 \\ 0 & \frac{u^\rho}{\rho_m} & 0 \\ 0 & 0 & 0 \end{bmatrix}. \tag{37}$$

For this example we define the material configuration through the inner and external radii $r_i = 5.6\,\text{mm}$ and $r_e = 7\,\text{mm}$, respectively. An homogeneous compressible Neo-Hookean material is considered, for which the strain energy function is given by

$$\Psi = C_1 \left(\overline{I}_1 - 3\right) + k_{vol} \left(J - 1\right)^2, \tag{38}$$

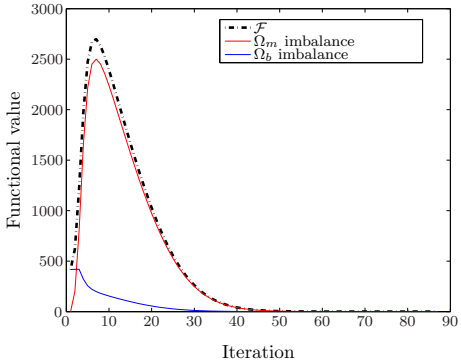

(a) Minimization of cost functional $\mathcal{F}$ and its components related to the mechanical imbalance at Ω_m and Ω_b. Shown values for the cost functional and components already include weighting factors $\eta_m = 1$ and $\eta_b = 100$.

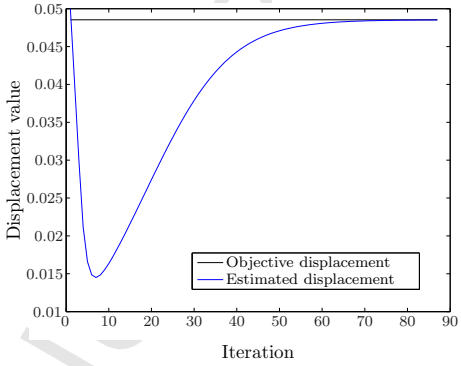

(b) Convergence of the resulting displacement for the load application point P through the minimization process. The objective value is $v_m(L) = 0.0485$.

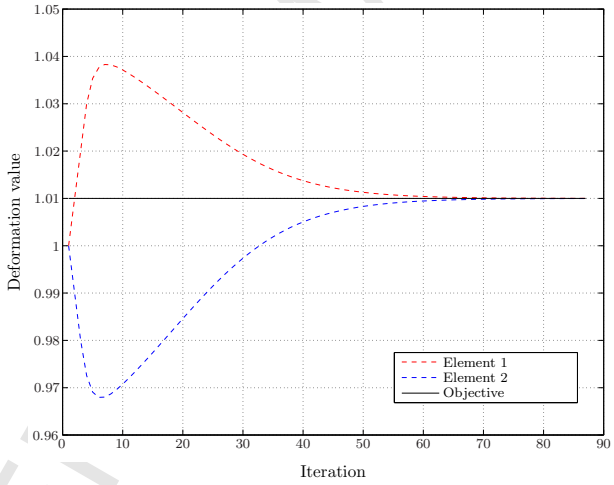

(c) Convergence of RRDs at each finite element. Target value for both elements (black horizontal line) and values estimated at each element through the minimization process (red and blue).

Figure 3: Results summary for the RRD characterization problem: 1D clamped bar example.

where $\bar{I}_1 = J^{-2/3}\mathrm{tr}\,(\mathbf{C})$, $J = \det \mathbf{F}$ are invariants of the deformation gradient tensor, and C_1 and k_{vol} represent shear and bulk material parameters, respectively. In this example, the constitutive parameters are set to $C_1 = 15\,\mathrm{kPa}$ (inspired by the values for the media layer presented in [5]) and $k_{vol} = 365\,\mathrm{kPa}$, (corresponding to a Poisson coefficient $\nu = 0.46$).

In this cylinder, the target RSs and RRDs are defined based on a continuous RS field of the following form

$$\boldsymbol{\sigma}^r(\rho_m) = \begin{bmatrix} \sigma^r_{m,\rho}(\rho_m) & 0 & 0 \\ 0 & \sigma^r_{m,\theta}(\rho_m) & 0 \\ 0 & 0 & \sigma^r_{m,z}(\rho_m) \end{bmatrix}, \quad (39)$$

where a linear form for $\sigma^r_{m,\theta}$ is considered and $\sigma^r_{m,\rho}$ is obtained as solution of the equilibrium at Ω_m. The RRD field is defined such that the objective stresses are generated considering the proposed constitutive behavior. The axial component of the stress field $\sigma^r_{m,z}$ is obtained from the defined RRD field. Note that $\sigma^r_{m,z}$ exerts no internal virtual power. Figure 4 displays the objective RS and RRD fields.

5.2.2. Manufactured solution

In order to construct the known setting for the identification problem we approximate the radial displacement field using 1D linear finite elements. The discretization is performed with 16 equally-sized elements. Piecewise constant RRDs are considered within each element. The value for each component of the RRD field is taken such that the associated internal power is equivalent to the corresponding for the continuous target field.

The mechanical equilibrium problem is solved for different values of internal pressure, $p_a = 1\,\mathrm{kPa}$, $p_b^1 = 2\,\mathrm{kPa}$ and $p_b^2 = 3\,\mathrm{kPa}$, to obtain the equilibrium configurations Ω_a, Ω_b^1 and Ω_b^2, respectively. The action of the internal pressure is introduced as a Neumann boundary condition in the corresponding node. The linearization of this problem is performed following the ideas presented in [8]. Observe that since the gradient operators (see ∇_m in (37)) depend on ρ, associated quantities (e.g. stresses, deformation gradient tensors) are not uniform within each element.

Figure 5(c) displays a representative scheme of the problem, highlighting geometrical landmarks (inner and external radii) for the involved configurations. In this context, Figure 5(a) shows the radial displacement fields w_m^1 and w_m^2 mapping Ω_a into Ω_b^1 and Ω_b^2 for an 8 finite elements discretization. Additionally, Figure 5(b) shows the displacement fields obtained for a fixed internal pressure $p = 1\,\mathrm{kPa}$. These figures illustrate the convergence of the finite element method.

Next, assuming Ω_a, Ω_b^1, Ω_b^2, $\mathbf{w}^1$ and $\mathbf{w}^2$ along with the equilibrating internal pressures p_a, p_b^1 and p_b^2 given as input data, the RRD identification will be addressed.

5.2.3. Optimization problem

For this problem we make use of the implementation of the interior-point algorithm available in the MATLAB Optimization Toolbox through the function *fmincon*. For the configuration options see AppendixA. As a constraint, a functional depending on the determinant of the RRD at each element is incorporated, assuming the form

$$\mathcal{C} = \sum_e (\det \mathbf{F}_m^{r,e} - 1). \quad (40)$$

Analogously to the numerical approximation employed for manufacturing the solution, 1D linear finite elements are used to approximate the radial displacement field and piecewise constant RRDs are considered within each element. Three different discretization levels are tested, using 2, 4 and 8 finite elements of equal size. For the setting of the initial conditions we consider $\mathbf{F}_a^r = \mathbf{I}$ for every case.

Three stages of optimization are used with a different set of weighting factors (η_m, η_b^1, η_b^2) each time; for the second and third optimization stages initial conditions are taken from the previous run. For the first optimization stage, weights are set as $\eta_b^1, \eta_b^2 = 100$ and $\eta_m = 0.1$. For the second stage weighting factors are $\eta_b^1, \eta_b^2 = 1$ and $\eta_m = 0.1$. Finally, $\eta_b^1 = \eta_b^2 = \eta_m = 1$ is considered for the last stage. Evaluation of the cost functional is performed using 4 Gauss points.

Since we consider $\mathbf{F}_a^r = \mathbf{I}$ as initial condition, the component of the functional $\mathcal{J}$ associated to the imbalance of the material configuration will be null and any perturbation of the RRD field near this initial point would increase such quantity. Taking this into account it is of paramount importance to choose the weighting parameters in the first stage such that the disequilibrium of the known configurations Ω_b^1 and Ω_b^2 is taken into account. To depict this fact, Figure 6(a) shows the variation of the functional $\mathcal{J}$ when a single variable is perturbed from the initial conditions if the weighting parameters $\eta_b^1 = \eta_b^2 = \eta_m = 1$ are considered (case with 2 finite elements). Additionally, Figure 6(b) shows the same variation when the parameters presented for the first stage are taken, showing that the initial condition $\mathbf{F}_a^r = \mathbf{I}$ no longer represents a local minimum.

It is also important to observe that, as the fields $\mathbf{w}^1 : \Omega_a \to \Omega_b^1$ and $\mathbf{w}^2 : \Omega_a \to \Omega_b^2$ (see Figure 1) are considered known only at the nodes (for each case) an error in the input data is being introduced. The relative discrepancies (measured in the L^2 norm) between the fields $\mathbf{w}^1$ and $\mathbf{w}^2$ generated in the manufacturing process and the ones given as input data for the optimization problem are $1.3 \cdot 10^{-3}$, $3.02 \cdot 10^{-4}$ and $6.05 \cdot 10^{-5}$ for the cases with 2, 4 and 8 finite elements, respectively.

5.2.4. Results

Figure 7 shows the minimization of the cost functional $\mathcal{F}$ along the three optimization stages for the three proposed levels of spatial discretization. The shown functional values have been normalized considering $\eta_b^1 = \eta_b^2 = \eta_m = 1$. In each case, the minimization algorithm stopped due to changes in every optimization variable below the minimum tolerance value of 10^{-10} (default value for the *fmincon*

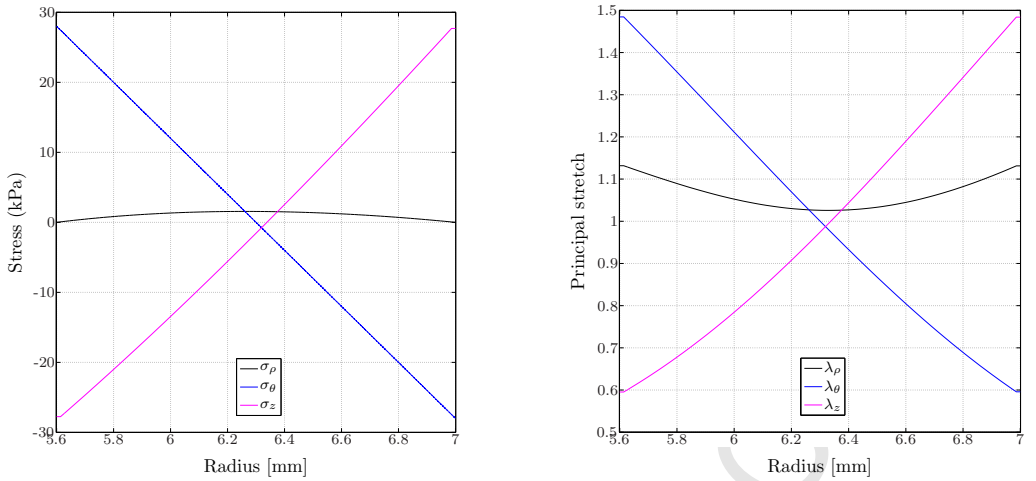

(a) Proposed residual stress field.

(b) Principal stretches defining the objective RRD field.

Figure 4: Thick-walled cylinder example: objective residual deformations and stresses

function provided in the MATLAB Optimization Toolbox [38]).

Figure 8 presents the results of the obtained RSs for each case, displaying a comparison between the results and their corresponding objective values. Similarly, Figure 9 presents the identified RRD fields. In these figures it can be observed that the proposed methodology is able to adequately characterize the RRDs in the cylinder. Also, the increasing number of elements in the spatial discretization consistently leads to a better identification of the target fields.

Table 1 summarizes the results for this problem, showing the discrepancy between the obtained results and target solutions. Here, e_σ indicates the relative discrepancy in RSs and $e_{\mathbf{F}^r}$ the corresponding relative discrepancy in RRDs measured in the L^2 norm. Additionally, e_v measures in the L^2 norm the relative discrepancy between the obtained radial displacement field v (mapping of Ω_m onto Ω_a) and the corresponding field obtained in the manufacturing of the known setting considering the target RRD field (and using a spatial discretization with 16 finite elements). As observed in Figures 7 and 8, the quality of agreement between the target data and the obtained results improves as more elements are incorporated. Finally, the total number of iterations and the achieved values of the cost functional are also shown. Furthermore, to provide a fair comparison between the obtained cost functionals, the cost functional corresponding to the results of the RRDs estimation achieved using the 2 and 4 finite elements were also evaluated using the finite element basis corresponding to the case with 8 finite elements (i.e. the test functions Φ_i in (23)-(23) are given by the linear shape functions associated to the 9 nodes of the 8 finite element discretization). The cost functional values obtained through this procedure are denoted by $\mathcal{J}^8$.

5.2.5. Discussion

Good results were obtained in this example, delivering a proper estimation of the morphology and magnitude of the target fields. We highlight that the material configuration is identified with great accuracy (through the radial displacement field) as the discrepancy with the objective data is of the same order of magnitude as the error given in the input data through the fields w^1 and w^2. This is verified for the three different discretization levels. Moreover, the use of finer approximations for the displacement field (and for the measure of the mechanical imbalance) consistently improves the quality of the obtained estimations.

Observe that each case features the minimization of a different cost functional as the definition of the functional $\mathcal{J}$ differs for each discretization in the number of shape functions used for the evaluation of the mechanical equilibrium. The cost functional $\mathcal{J}^8$ associated with the finer discretization offers the best evaluation of the mechanical imbalance of the obtained results. As it can be noted in Table 1 the value of this cost functional presents a correlation with the quality of the estimation.

An important issue regarding the choice of weighting parameters η_m and η_b^j can be appreciated in this example. Figure 6 suggests the existence of possibly several local minima and shows that the modification of weighting parameters can provide a successful exit path for the functional minimization. This motivated the use of the three optimization stages, were weighting parameters are modified in order to reshape the cost functional and avoid the stagnation of the minimization process.

5.3. Three-layered arterial wall

5.3.1. Problem description

In this example, RRDs resembling the setting of an abdominal aortic wall are characterized. For modeling purposes, a simplified cylindrical arterial wall configuration

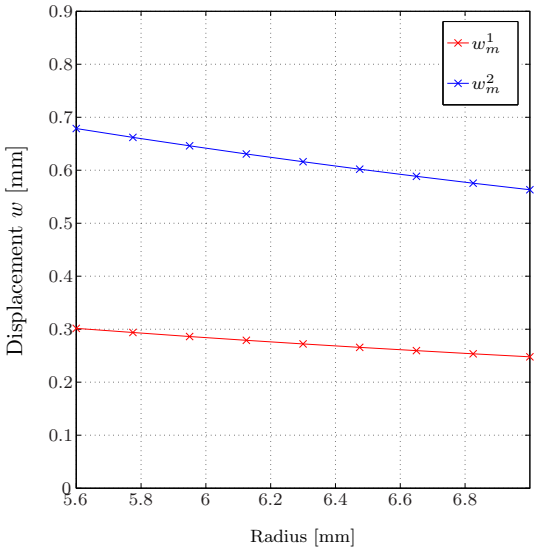

(a) Radial displacement fields w_m^j mapping Ω_a into Ω_b^j for the 8 finite element discretization.

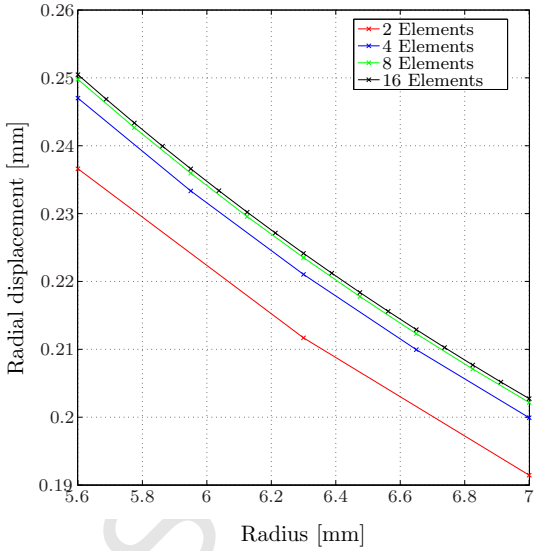

(b) Solution of the mechanical problem with $p = 1\,kPa$. Displacement field obtained for the different discretization levels expressed terms of material coordinates.

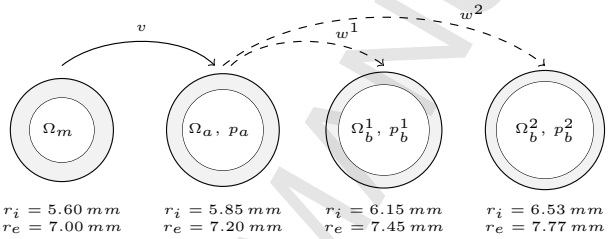

(c) Problem representative scheme

Figure 5: Thick-walled cylinder example: results for the mechanical problem

Elements	e_σ	$e_{\mathbf{F}^r}$	e_v	$\mathcal{J}$	$\mathcal{J}^8$	Iterations
2	$5.27{\cdot}10^{-1}$	$1.03{\cdot}10^{-1}$	$7.77{\cdot}10^{-3}$	$1.26{\cdot}10^{-1}$	$3.56{\cdot}10^{+1}$	231
4	$2.61{\cdot}10^{-1}$	$5.11{\cdot}10^{-2}$	$2.30{\cdot}10^{-3}$	$2.68{\cdot}10^{-2}$	$2.65{\cdot}10^{+1}$	546
8	$1.89{\cdot}10^{-1}$	$3.29{\cdot}10^{-2}$	$4.47{\cdot}10^{-5}$	$6.85{\cdot}10^{-2}$	$6.85{\cdot}10^{-2}$	948

Table 1: Thick-walled cylinder example: identification error summary.

with uniform thickness is assumed. As a consequence, the kinematic setting for this problem is the same is the same as the one introduced in Section 5.2.1. In contrast to the previous example, the wall consists of three layers of uniform thickness (see Table 2), each. Arterial tissue in each layer features uniform properties and is assumed to behave as a hyperelastic quasi-incompressible material characterized by the following strain energy function (see [1]):

$$\Psi = \frac{c}{2}(\overline{I}_1 - 3) + \frac{k_1}{2k_2}\sum_{i=4,6}\delta_i\left\{e^{k_2(\overline{I}_i-\lambda_i^0)^2} - 1\right\} + k_{vol}(J-1)^2. \quad (41)$$

In this context, k_{vol} is the bulk modulus, $J = \det\mathbf{F}_m$ and $\overline{\mathbf{F}}_m = \mathbf{F}_m J^{-1/3}$ is the isochoric deformation tensor. Associated to this deformation we have $\overline{\mathbf{C}}_m = \overline{\mathbf{F}}_m^T\overline{\mathbf{F}}_m$ and the isochoric invariants

$$\overline{I}_1 = \mathbf{I}\cdot\overline{\mathbf{C}}_m, \qquad \overline{I}_i = \overline{\mathbf{C}}_m\cdot(\mathbf{a}_i\otimes\mathbf{a}_i),\ i = 4,6, \quad (42)$$

where $\mathbf{a}_i$, $i = 4,6$ are the unit vectors indicating the orientation of the collagen fibers. It is worthwhile to mention that recruitment stretches λ_i^0 are defined in such a way that in the material configuration collagen fibers store null energy, i.e.

$$\lambda_i^0 = \overline{\mathbf{C}}_m^r\cdot(\mathbf{a}_i\otimes\mathbf{a}_i), \qquad \overline{\mathbf{C}}_m^r = \overline{\mathbf{F}}_m^r(\overline{\mathbf{F}}_m^r)^T. \quad (43)$$

This fact implies that the collagen load bearing starts when the vessel is inflated beyond the null pressure level and they have no influence in the RS state induced by RRDs. This assumption is motivated by the remodeling process experienced by the collagen [41] (through continuous degradation and synthesis), enabling the adoption of

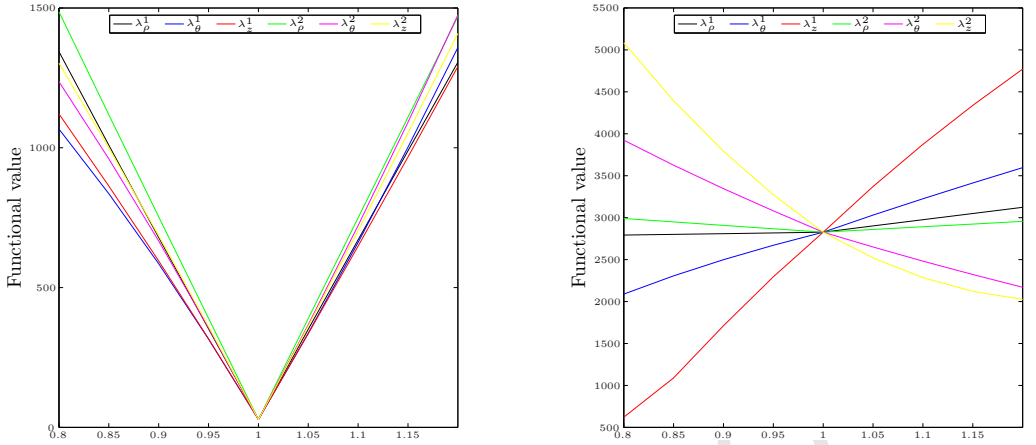

(a) Weighting parameters $\eta_m = \eta_b^1 = \eta_b^2 = 1$

(b) Weighting parameters $\eta_b^1 = \eta_b^2 = 100$ and $\eta_m = 0.1$

Figure 6: Thick-walled cylinder example: functional values resulting from the perturbation of a single optimization variable in the initial conditions $\mathbf{F}_a^r = \mathbf{I}$, for the case with 2 finite elements. Supra-index indicates the number of the element to which the variable is related to and the line colors identify the perturbed variable in each case.

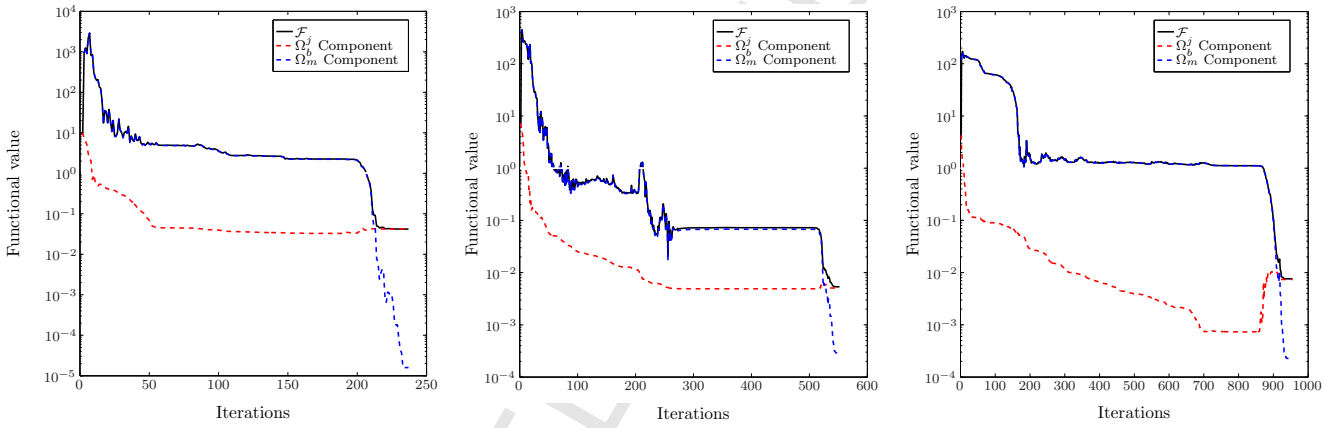

(a) 2 Finite elements (b) 4 Finite elements (c) 8 Finite elements

Figure 7: Thick-walled cylinder example: minimization process showing functional value for the three optimization stages. Functional values are corresponding to normalized weights $\eta_b^1 = \eta_b^2 = \eta_m = 1$.

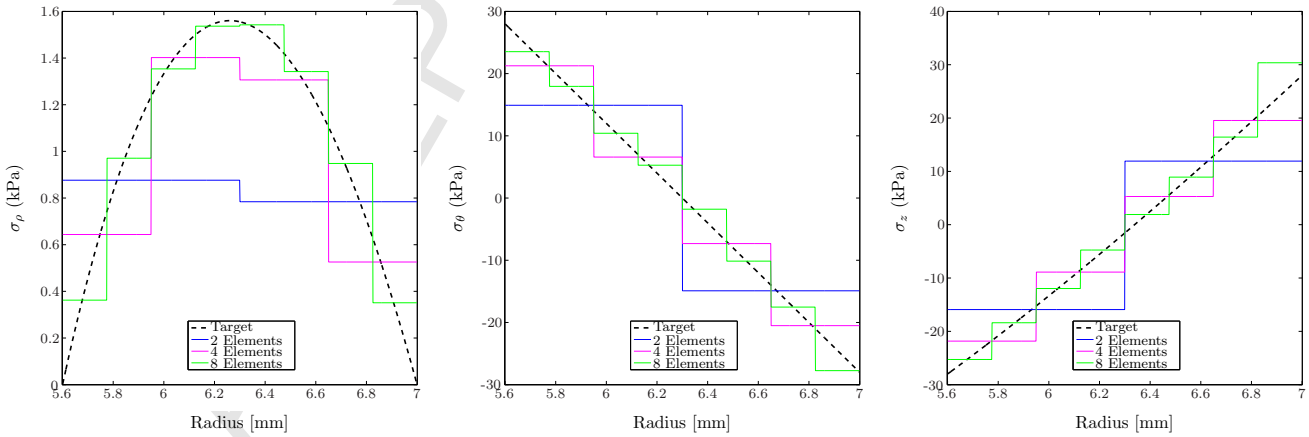

(a) Radial component (b) Tangential component (c) Axial component

Figure 8: Thick-walled cylinder example: residual stresses for different discretization levels. Comparison between obtained results (colored solid lines) and target field (dashed).

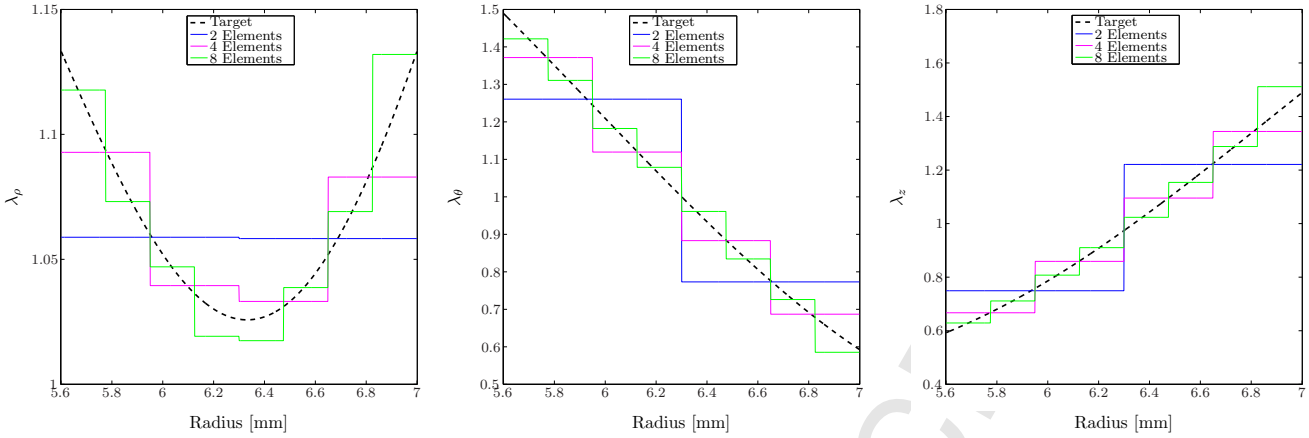

(a) Radial component (b) Tangential component (c) Axial component

Figure 9: Thick-walled cylinder example: principal stretches characterizing the RRDs for different discretization levels. Comparison between obtained results (colored solid lines) and the target field (dashed).

different configurations of the fibers and avoiding the existence of RRDs in the material configuration.

These scenarios are proposed to evaluate the capabilities of the identification problem to deliver the correct RRDs as the amount of input data is increased.

Based on experimental measurements for each individual layer (data available in [7]), [5] proposed a methodology to define a field of RRDs (here denoted $\mathbf{F}_m^{exp}$). This RRD field is expressed in terms of the components λ_ζ, $\zeta \in (\rho, \theta, z)$, adopting the following forms for each of the corresponding layers

$$\mathbf{F}_m^{exp,(I)} = \begin{pmatrix} \lambda_{\rho_m}^{(I)} & 0 & 0 \\ 0 & \lambda_\theta^{(I)} & 0 \\ 0 & 0 & \lambda_z^{(I)} \end{pmatrix},$$

$$\mathbf{F}_m^{exp,(M)} = \begin{pmatrix} -\lambda_{\rho_m}^{(M)} & 0 & 0 \\ 0 & 0 & \lambda_\theta^{(M)} \\ 0 & \lambda_z^{(M)} & 0 \end{pmatrix},$$

$$\mathbf{F}_m^{exp,(A)} = \begin{pmatrix} \lambda_{\rho_m}^{(A)} & 0 & 0 \\ 0 & \lambda_\theta^{(A)} & 0 \\ 0 & 0 & \lambda_z^{(A)} \end{pmatrix}, \tag{44}$$

where and superscripts $(I), (M), (A)$ indicate that the field corresponds to the intima, media or adventitia layer, respectively. The dependence of the fields with respect to ρ_m is not explicitly indicted for the sake of readability. Note that these components are related to the principal values for the associated Cauchy-Green deformation tensor, given by

$$\mathbf{C}_m^{exp} = \begin{bmatrix} \lambda_\rho^2 & 0 & 0 \\ 0 & \lambda_\theta^2 & 0 \\ 0 & 0 & \lambda_z^2 \end{bmatrix}. \tag{45}$$

The values for the components of the RRD field and the associated RSs proposed in [5] (where the complete functional form for each component and layer is reported) take the form shown in Figure 10.

Material parameter	Intima	Media	Adventitia
Thickness [mm]	0.30	0.81	0.32
c [kPa]	39.8	31.4	17.3
k_{vol} [10^2 kPa]	4.84	3.82	2.10
k_1[MPa]	10.1	0.81	0.98
k_2	0.01	12.4	3.35
β [°]	40.5	39.1	40.6

Table 2: Summary of material parameters for the three-layered wall example

The material parameters characterizing the isotropic term of the strain energy function are also taken from [5]. The bulk moduli are consistent with a Poisson modulus $\nu = 0.46$, considering that the volumetric stiffness is determined by the isotropic contribution. Parameters characterizing the behavior of the two collagen fiber families are taken from [4]. Table 2 summarizes the material behavior parameters for this problem.

5.3.2. Manufactured solution

With the material configuration and RRDs already defined, the mechanical problem is solved for different levels of inner pressure ($p = 6$ kPa and $p_b^j = 8, 10, 12, 14$ kPa, with $j = 1, 2, 3, 4$) to construct the known setting for the RRD identification problem. The obtained equilibrium configurations are denoted as Ω_a and Ω_b^j, respectively. Analogously to the previous example, linear 1D finite elements are used to approximate the radial displacement field and piecewise constant RRDs are considered within each element. As before, the value for each component of the RRD field is taken such that the associated internal power is equivalent to the corresponding for the continuous target field. The discretization considered for the manufacturing process consists of 16 finite elements, with 4 elements for the intima layer, 8 for the media and 4 for the adventitia. Elements are of equal size within each layer.

Figure 11(c) displays a representative scheme of the problem, while Table 3 presents the geometrical landmarks for the involved configurations in scenario (d). Figure 11(a) shows the radial displacement field obtained for an inner pressure $p = 6\,\text{kPa}$, while Figure 11(b) shows the radial displacement fields w_m^j for each of the four additional known configurations proposed in scenario (d). The numerical integration is performed using 4 Gauss points.

5.3.3. Optimization problem

As before, for the spatial discretization 1D linear finite elements are used to approximate the radial displacement field and piecewise constant RRDs are considered within each element. Two different discretization levels are tested, using 3 and 8 finite elements. For the first case, a unique finite element will represent each layer, while for the second case we consider 2, 4 and 2 elements for the intima, media and adventitia layers, respectively. Within each layer, elements are of equal size.

In order to evaluate the influence of the amount of known data, four scenarios are analyzed, where Ω_a is considered to be the solution of the forward problem obtained for an internal pressure $p_a = 6\,\text{kPa}$. In addition to this known Ω_a configuration, for each scenario a different number of additional known configurations is considered, according to the following

(a) 1 additional configuration (at equilibrium with $p = 8$ kPa),

(b) 2 additional configurations (at equilibrium with $p = 8/10$ kPa),

(c) 3 additional configurations (at equilibrium with $p = 8/10/12$ kPa),

(d) 4 additional configurations (at equilibrium with $p = 8/10/12/14$ kPa).

As noted for the previous example, as the fields w^j will be considered known only at the corresponding nodes, an error in this field is incorporated in the input data. In this example, the discrepancies (measured in the L^2 norm) between the w^j fields generated in the manufactured process and the same fields given as input data ascends up to $2.2 \cdot 10^{-3}$ and $1.24 \cdot 10^{-4}$ for the 3 and 8 finite elements discretizations, respectively.

As a constraint, a functional depending on the determinant of the RRD for each element is considered. This constraint is expressed as

$$\mathcal{C} = \sum_e (\det \mathbf{F}_m^{r,e} - 1)^2 < \varpi, \tag{46}$$

with $\varpi = 0.01$.

When tackling the problem with the 3 finite element discretization we consider $\mathbf{F}_a^r = \mathbf{I} \cdot 1.01$ as initial condition for each scenario. Three stages of optimization are used, using a different set of weighting parameters each time (see below). For the first optimization stage the aforementioned initial condition is given, then for the second and third optimization stages, the initial condition is given by the result achieved at the previous stage.

Once the solution is achieved for each proposed scenario using the coarse discretization, the problem is solved again using the finer discretization. As before, three stages of optimization are used. For each scenario, we consider as initial condition the result obtained with the 3 finite element discretization. This initial condition is given as input for the first optimization stage. Next, for the second and third optimization stages, the initial conditions are given by the result achieved at the previous stage.

For both discretizations the following weights are used: $\eta_m = 0.1$, $\eta_{b,j} = \frac{10}{N}$ for the first stage, $\eta_m = 10$, $\eta_{b,j} = \frac{1}{N}$ for the second stage, and $\eta_m = 1$, $\eta_{b,j} = \frac{1}{N}$ for the third stage. Note that $j = 1, \ldots, N$, with N representing the number of known configurations -additional to Ω_a- (see list of scenarios in Section 5.3.1) for the corresponding case. Several combinations of weighting parameters were tested for these optimization routines, the chosen values were determined by selecting the combination that provides the minimum average for the resulting cost functional values.

For all the optimization stages listed the options setting for the MATLAB *fmincon* is presented in AppendixA. The integration required for the numerical computation of the preload problem and the evaluation of generalized residuals is performed using 4 Gauss points in each element.

5.3.4. Sensitivity with respect to material parameters

A sensitivity analysis is presented to study the impact of imperfect input data in the characterization of the RRD and RS fields. This is done by considering perturbations in the material parameters. Particularly, the attention is focused in the parameter c (see 41), and the results obtained for a group of 27 perturbed input data sets are analyzed. These perturbed sets are constructed considering all possible combinations assuming that each layer could present its correct value or a deviation (positive or negative) of 5% of its actual value.

All the numerical tests regarding this analysis are done using the coarser discretization consisting of one finite element per layer. The same configuration presented for the coarser discretization is used in each case.

5.3.5. Results

Results for the 3 finite elements discretization. An overview of the results for the four proposed scenarios is presented in Table 4, where the identification errors are summarized. Here, the number of functional evaluations for each scenario and the value achieved for the cost functional $\mathcal{J}$ (normalized with $\eta_{b,j} = \frac{1}{N}$, $\eta_m = 1$) are shown. Additionally, $\mathcal{J}^d$ stands for the functional value that is achieved evaluating the corresponding solutions with the functional form associated to scenario (d), i.e. considering 4 additional known configurations. Like in the previous

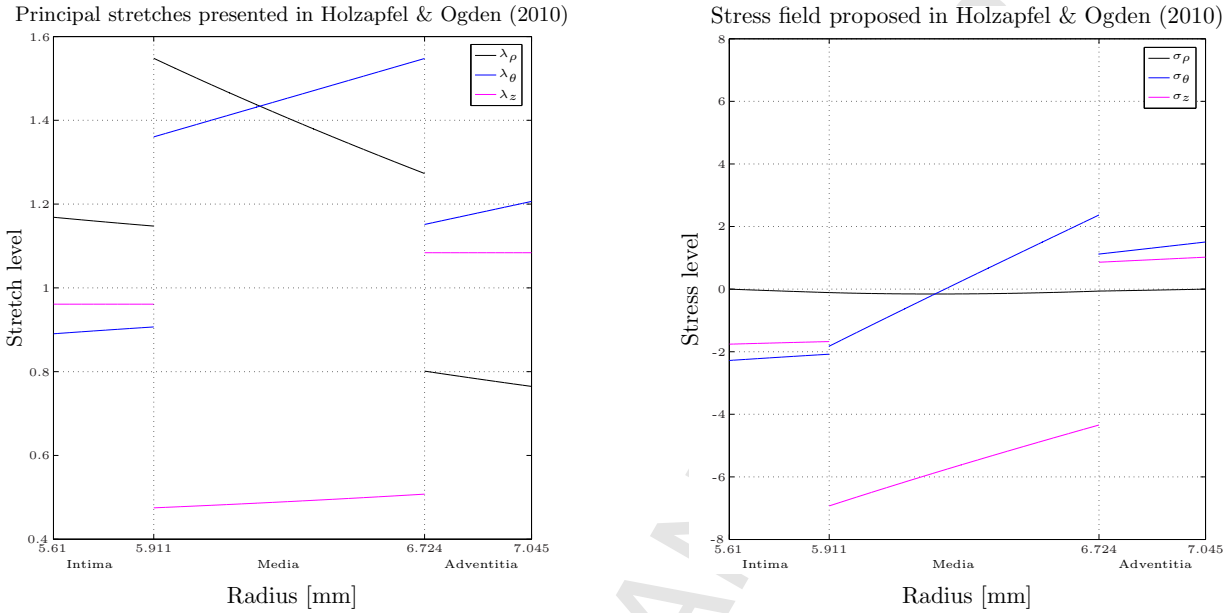

(a) Components of the RRD field.

(b) Residual stress field.

Figure 10: Components λ_ζ, $\zeta \in (\rho, \theta, z)$ shaping the RRD field and the associated residual stresses through the wall radius as introduced in [5].

Three-layered aorta: geometrical landmarks of manufactured solution for scenario (d)					
Configuration	Pressure [kPa]	Inner radius [mm]	Intima thickness	Media thickness	Adv. thickness
Ω_m	0	5.61	0.301	0.813	0.321
Ω_a	6	6.05	0.280	0.781	0.306
Ω_b^1	8	6.12	0.277	0.779	0.304
Ω_b^2	10	6.18	0.274	0.778	0.303
Ω_b^3	12	6.23	0.272	0.778	0.302
Ω_b^4	14	6.28	0.259	0.778	0.301

Table 3: Three-layered aorta example: geometrical landmarks.

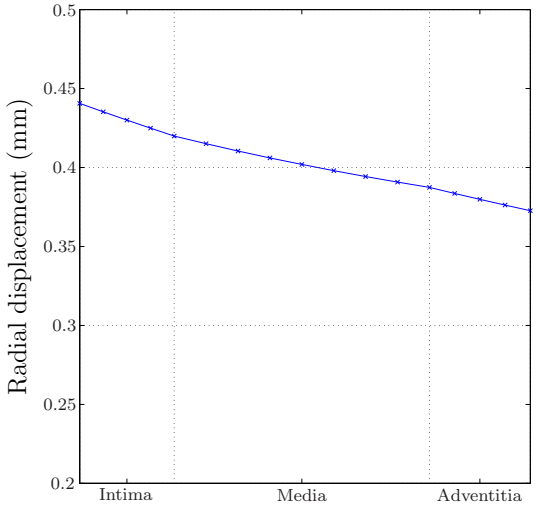

(a) Displacement fields obtained as solution of the forward problem for internal pressure $p = 6\,\text{kPa}$ obtained in the manufacturing process.

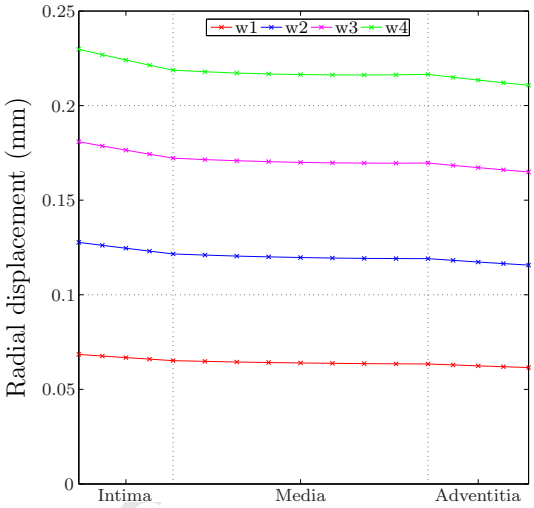

(b) Radial displacement fields w_m^j mapping Ω_a onto Ω_b^j, $j = 1, 2, 3, 4$ for the set of known configurations proposed in scenario (d).

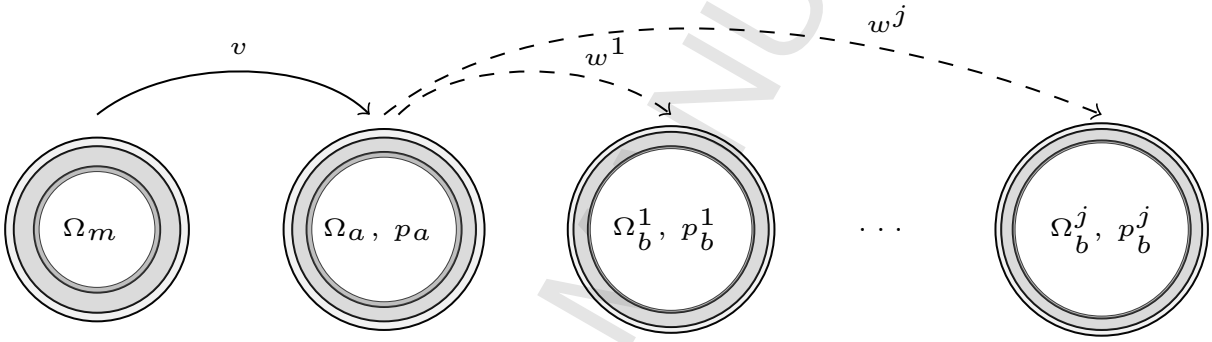

(c) Schematic setting for the problem.

Figure 11: Numerical solution of the forward mechanical problem.

example, error measures for the RRDs, RSs and displacement fields are presented.

As can be seen in Table 4, if at least one additional known configuration is given as input data a noticeable decrease in the discrepancy between the results and target data is obtained. Focusing on scenarios (a) and (d), it is shown that the discrepancies with the objective data (measured in the L^2 norm) decrease from $3.70 \cdot 10^{-1}$ to $2.38 \cdot 10^{-1}$ for the RS field, from $1.29 \cdot 10^{-1}$ to $7.77 \cdot 10^{-2}$ for the RRD field and from $3.18 \cdot 10^{-3}$ to $8.81 \cdot 10^{-4}$ for the displacement field v mapping Ω_m into Ω_a. From the reported values for the cost functional $\mathcal{J}^d$, in this example it is observed that smaller values do not necessarily indicate a better agreement with the target data.

Figure 12 features a comparison between the obtained values for the components of the RRD field, for the four proposed scenarios and the objective fields reported in [5]. From this figure it can be noted that scenarios (b) to (d) offer a good estimation of the mean value for all the components of the deformation tensor in the intima and media layers and for the circumferential component in the adventitia. All scenarios fail at presenting accurate estimations for the radial and axial components in the adventitia, and scenario (b) presents the best results regarding this target variable. Although results obtained in scenario (a) are clearly poorer than the others, they still offer a good approximation for the circumferential component in the media and adventitia, and the axial deformation components in the media.

Additionally, Figure 13 presents a similar comparison for the obtained RS field. In this figure it is shown that the better estimation in RRDs offered by scenarios (b) to (d) is also reflected in the associated stress field. For these scenarios, it is interesting to note the great accuracy in the estimation (of the mean value) of the stresses in the intima layer for all the components. Furthermore, the circumferential and axial components for the media layer are also identified with great accuracy. As before, larger errors are observed in the characterization of the RS field for the adventitia layer.

Results for the 8 finite elements discretization. As before, an overview of the results for the four proposed scenarios

Scenario	e_σ	$e_{\mathbf{F}^r}$	e_v	$\mathcal{J}$	$\mathcal{J}^d$	Iterations
(a)	$3.70{\cdot}10^{-1}$	$1.29{\cdot}10^{-1}$	$3.18{\cdot}10^{-3}$	$1.93{\cdot}10^{-1}$	$4.29{\cdot}10^{-1}$	115
(b)	$2.28{\cdot}10^{-1}$	$6.84{\cdot}10^{-2}$	$3.71{\cdot}10^{-4}$	$1.45{\cdot}10^{-1}$	$2.55{\cdot}10^{-1}$	198
(c)	$2.66{\cdot}10^{-1}$	$8.78{\cdot}10^{-2}$	$8.07{\cdot}10^{-4}$	$4.91{\cdot}10^{-2}$	$5.90{\cdot}10^{-2}$	163
(d)	$2.38{\cdot}10^{-1}$	$7.77{\cdot}10^{-2}$	$8.81{\cdot}10^{-4}$	$1.21{\cdot}10^{-1}$	$1.21{\cdot}10^{-1}$	271

Table 4: Three-layered aorta example: summary of results corresponding to the 3 finite element approximation. Values for the functional $\mathcal{F}$ are normalized using $\eta_{b,j} = \frac{1}{N}, \eta_m = 1$ $(j = 1, \ldots, N)$.

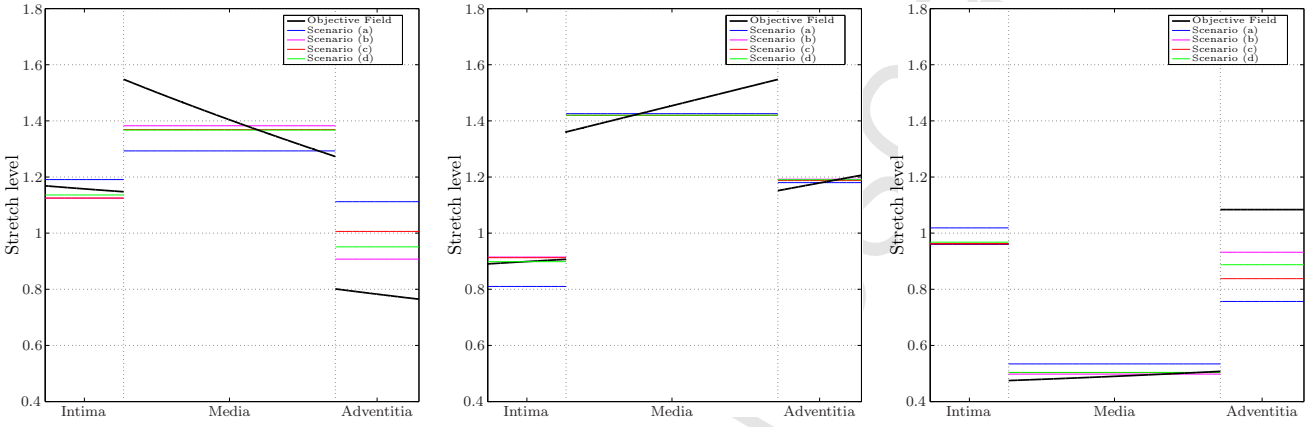

(a) Radial component. (b) Circumferential component. (c) Axial component.

Figure 12: Three-layered wall example: results for the 3 finite element approximation. Residual deformations obtained as result of the optimization process for the four proposed scenarios compared with the objective field.

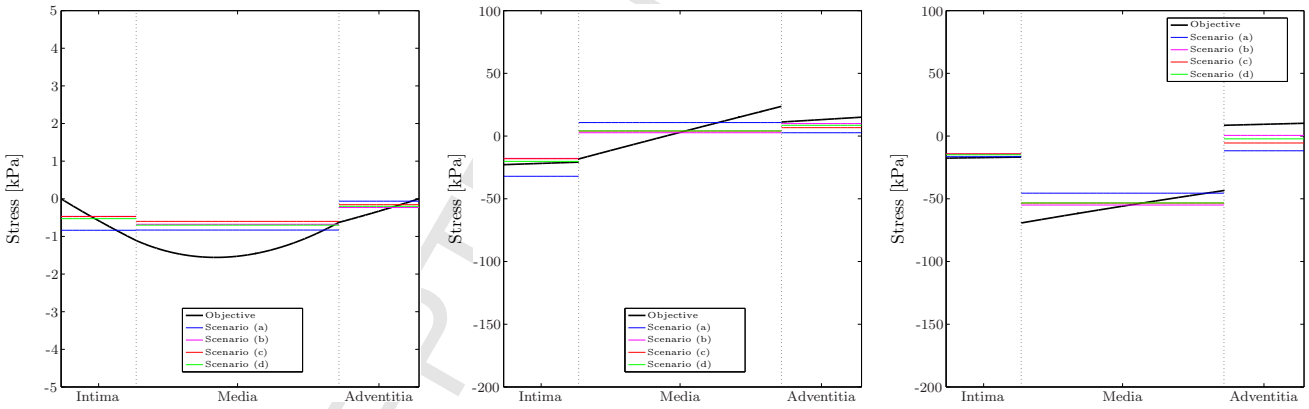

(a) Radial RS (b) Circumferential RS. (c) Axial RS.

Figure 13: Three-layered wall example: results for the 3 finite element approximation. Residual stresses arising from the residual deformation field obtained as result of the optimization process for the four proposed scenarios, compared with the target field.

Scenario	e_σ	$e_{\mathbf{F}^r}$	e_v	$\mathcal{J}$	$\mathcal{J}^d$	Iterations
(a)	$3.78{\cdot}10^{-1}$	$1.33{\cdot}10^{-1}$	$4.01{\cdot}10^{-4}$	$6.35{\cdot}10^{-2}$	$5.97{\cdot}10^{-1}$	161
(b)	$1.78{\cdot}10^{-1}$	$6.10{\cdot}10^{-2}$	$1.00{\cdot}10^{-3}$	$2.75{\cdot}10^{-1}$	$5.24{\cdot}10^{-1}$	161
(c)	$2.00{\cdot}10^{-1}$	$7.32{\cdot}10^{-2}$	$2.18{\cdot}10^{-3}$	$1.42{\cdot}10^{-1}$	$1.90{\cdot}10^{-1}$	157
(d)	$1.72{\cdot}10^{-1}$	$6.40{\cdot}10^{-2}$	$1.59{\cdot}10^{-3}$	$1.91{\cdot}10^{-1}$	$1.91{\cdot}10^{-1}$	178

Table 5: Three-layered wall example: summary of results corresponding to the 8 finite element approximation. Values for the functional $\mathcal{J}$ are normalized using $\eta_{b,j} = \frac{1}{N}, \eta_m = 1$ $(j = 1, \ldots, N)$.

is presented in Table 5, where the identification errors are summarized. Here, the number of functional evaluations for each scenario and the value achieved for the functionals $\mathcal{J}$ and $\mathcal{J}^d$ (both normalized with $\eta_{b,j} = \frac{1}{N}$, $\eta_m = 1$) are also shown.
Similarly to the results obtained with the coarser discretization, Table 5 shows that the incorporation of at least one additional known configuration contributes with the identification of the RRD ans RS fields, halving the magnitude of the discrepancies with respect to the target fields. Despite this, Scenario (a) unexpectedly provides the better estimation for the material configuration. From the presented discrepancy measures, it follows that the incorporation of additional data in the form of known configurations in scenarios (c) and (d) do not significantly contribute to improve the quality of the estimation. We remark that the identification errors associated with the RS and RRD fields improve with respect to the results achieved with the 3 finite element discretization. For example, for scenario (d) it is observed a reduction of approximately 27% and 17% for the RSs and RRDs, respectively. Although the relative errors associated to the radial displacement field display an increase in their value, they still present small magnitudes, in the order of $1 \cdot 10^{-3}$.

Figure 14 features a comparison between the obtained values for the components of the RRD field, for the four proposed scenarios and the objective fields reported in [5]. It is observed that the more important contribution of this finer discretization is the identification of the gradient of the circumferential component of the deformation field, particularly in the media and adventitia layers. The impact of the refined discretization on the estimation of the radial distribution of wall stresses is shown in Figure 15. A better estimation of the shape of the RS field can be noted not only in the circumferential components of the media and adventitia, but also in the general morphology on the radial components. Both figures highlight, again, that the most relevant discrepancies are primarily found in the adventitia layer.

Sensitivity with respect to material parameters. Table 6 summarizes the results for the 27 proposed cases for the assessment of the sensitivity with respect to material parameters. As before, the relative discrepancies with the target data measured in the L^2 norm together with the achieved functional values and the number of combined iterations for the three optimization stages are shown. The mean value of the discrepancies e_σ, $e_{\mathbf{F}^r}$ and e_v are $2.58 \cdot 10^{-1}$, $8.27 \cdot 10^{-2}$ and $5.51 \cdot 10^{-3}$, respectively. In the worst case scenario, discrepancies are up to $3.38 \cdot 10^{-1}$, $1.40 \cdot 10^{-1}$ and $1.03 \cdot 10^{-2}$ for the relative errors associated to the RS, RRD and displacement fields, respectively.

Additionally, Figure 16(a) summarizes the results for the 27 proposed cases, displaying the average of the reported values for the components shaping the RRD field and the associated standard deviation. These results are compared with the average deformation components in each layer. Similarly, Figure 16(b) shows the comparison between the resulting stresses in each layer and the mean in each layer associated with the objective field.

5.3.6. Discussion

From a general point of view, valuable results were achieved identifying the mean value of the components of stresses and deformations in the arterial wall. Remarkably, these results can be achieved using a 3 finite element model that discretized each layer with only one element. Moreover, using the 8 finite element discretization it was possible to obtain an approximation of the morphology of the fields, as it is clearly observed for the radial and circumferential stresses in Figure 15. Identifiability of residual deformations is encouraging for the intima and media layer, however, the characterization of the adventitia layer is particularly challenging because of its high compliance. As a consequence, the proposed cost functional features a smaller sensitivity with respect to changes in the corresponding optimization variables. Another interesting fact is that the relatively small value of the radial component of the stress field seems to be an obstacle for it to be identified.

Overall, if at least 3 configurations and the displacements w^j at four geometrical landmarks [3] are known, it is possible to obtain a good estimation of the RRDs in the more mechanically relevant layers (in this example, the intima and media). In particular, the results show a good estimation of the mean value of the circumferential and axial components of the stresses in the intima and media layers. It is remarkable that in each scenario the relative error in the identification of the displacement field is smaller than that one introduced in the displacements w^j due to the use of interpolated input data.

In contrast, it is not promising the fact that, in this example,smaller values of the cost functional (see $\mathcal{J}^d$ in Tables 4 and 5) are not consistently related to improved quality of estimated variables. It is also shown that additional information (knowledge of a 3rd or 4th deformed configuration) can result in an increase of the relative error of the estimated RRD, RS and displacement fields. These points can be partially explained by the fact that the incorporation of known configurations associated to higher pressure levels modifies the metric used to characterize the mechanical imbalance which drives the optimization. The internal virtual power associated to a configuration at equilibrium with an elevated pressure level will be naturally higher, and, as a result, the cost functional is, thus, more sensitive to a disequilibrium in such configuration. Furthermore, the convergence of the algorithm to local minima could also be influencing the final results.

Finally, the sensitivity analysis with respect to given material parameters shows that the discrepancies with the

[3] inner radius, internal elastic lamina, external elastic lamina and external radius

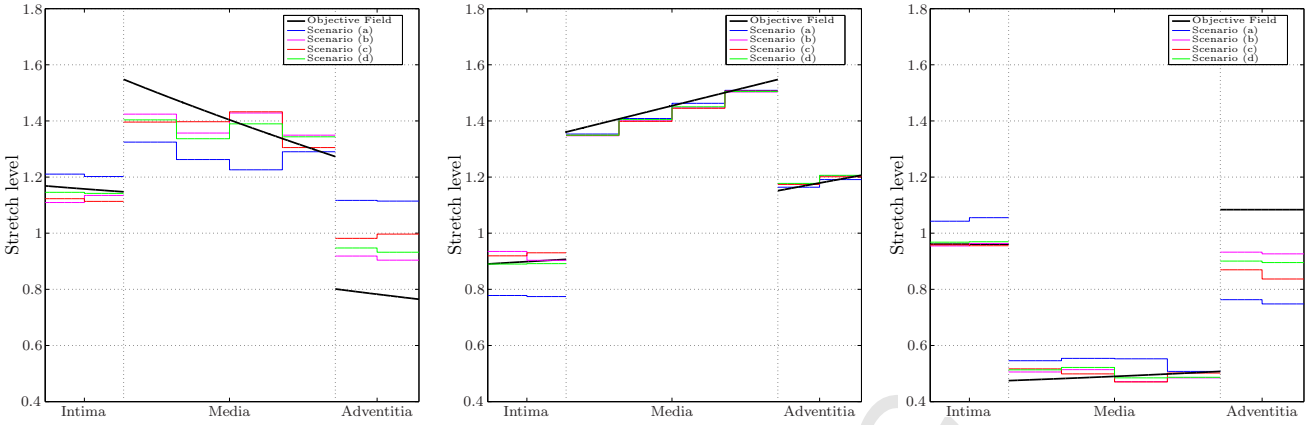

(a) Radial component. (b) Circumferential component. (c) Axial component.

Figure 14: Three-layered wall example: results for the 8 finite element discretization. Residual deformations obtained as result of the optimization process for the four proposed scenarios compared with the objective field.

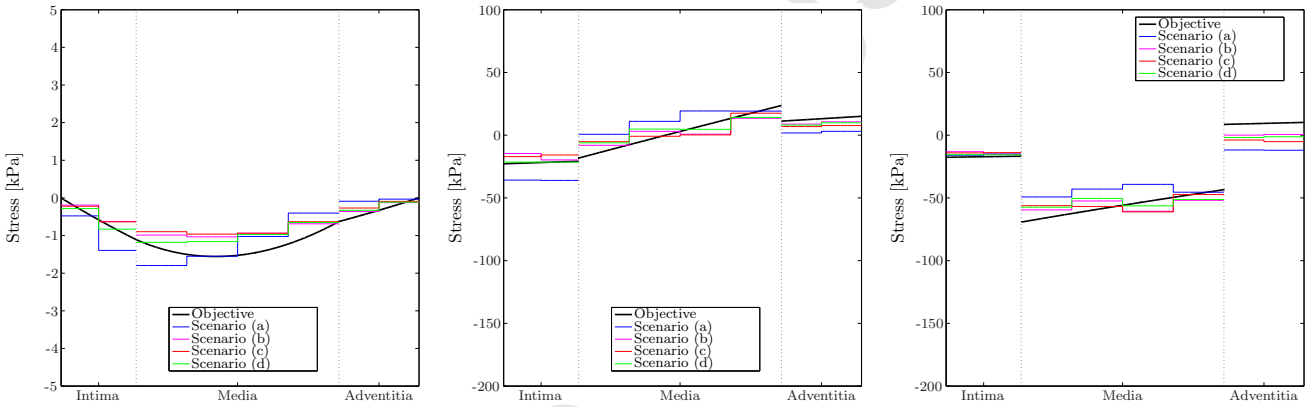

(a) Radial stress (b) Circumferential stress. (c) Axial stress.

Figure 15: Three-layered wall example: results for the 8 finite element approximation. Residual stresses arising from the residual deformation field obtained as result of the optimization process for the four proposed scenarios, compared with the target field.

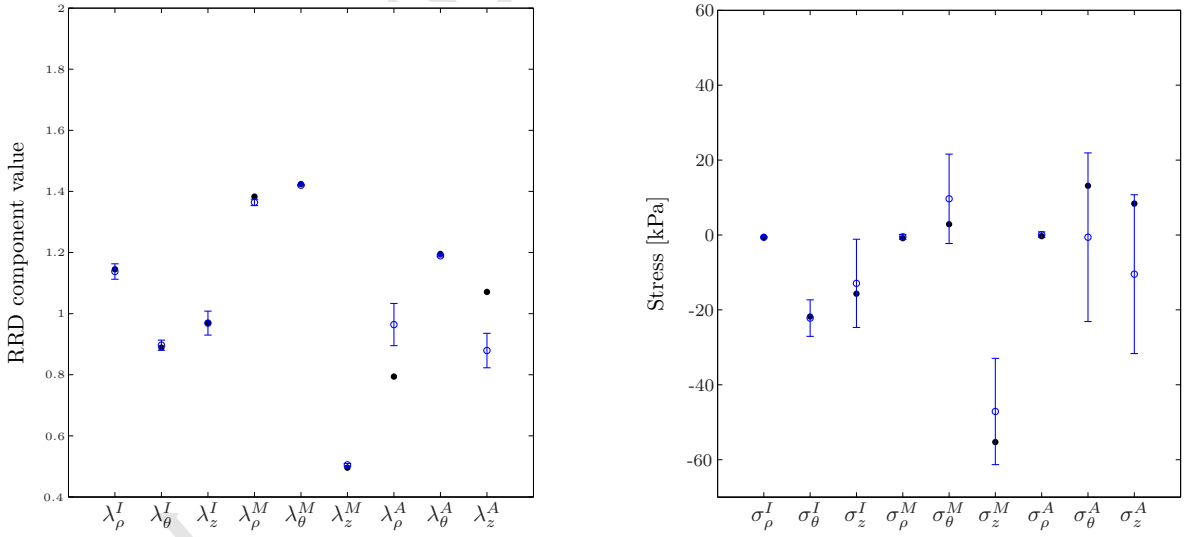

(a) Components of the RRD field for each layer. (b) Components of the RS field for each layer.

Figure 16: Results obtained for the material parameter sensitivity analysis. For each variable, blue circles indicate the mean value for the 27 analyzed cases while error bars indicate the associated standard deviation. Black dots point out target fields (mean value in each layer).

Variation of mat. par. c (%)			R				esults
Intima	Media	Adventitia	e_σ	$e_{\mathbf{F}^r}$	e_v	$\mathcal{J}$	Iterations
95	95	95	$2.66{\cdot}10^{-1}$	$8.53{\cdot}10^{-2}$	$8.97{\cdot}10^{-3}$	$1.97{\cdot}10^{-1}$	187
95	95	100	$2.42{\cdot}10^{-1}$	$7.46{\cdot}10^{-2}$	$9.21{\cdot}10^{-3}$	$1.12{\cdot}10^{-1}$	240
95	95	105	$2.30{\cdot}10^{-1}$	$6.87{\cdot}10^{-2}$	$8.42{\cdot}10^{-3}$	$1.93{\cdot}10^{-1}$	340
95	100	95	$2.69{\cdot}10^{-1}$	$9.30{\cdot}10^{-2}$	$1.65{\cdot}10^{-3}$	$1.50{\cdot}10^{-1}$	144
95	100	100	$2.43{\cdot}10^{-1}$	$8.06{\cdot}10^{-2}$	$1.44{\cdot}10^{-3}$	$4.96{\cdot}10^{-2}$	257
95	100	105	$2.28{\cdot}10^{-1}$	$7.27{\cdot}10^{-2}$	$1.46{\cdot}10^{-3}$	$6.99{\cdot}10^{-2}$	244
95	105	95	$2.62{\cdot}10^{-1}$	$9.10{\cdot}10^{-2}$	$6.28{\cdot}10^{-3}$	$1.66{\cdot}10^{-1}$	336
95	105	100	$2.36{\cdot}10^{-1}$	$7.64{\cdot}10^{-2}$	$6.21{\cdot}10^{-3}$	$7.10{\cdot}10^{-2}$	229
95	105	105	$2.49{\cdot}10^{-1}$	$8.23{\cdot}10^{-2}$	$7.25{\cdot}10^{-3}$	$1.69{\cdot}10^{-1}$	198
100	95	95	$2.58{\cdot}10^{-1}$	$8.38{\cdot}10^{-2}$	$9.87{\cdot}10^{-3}$	$2.85{\cdot}10^{-1}$	242
100	95	100	$2.35{\cdot}10^{-1}$	$7.19{\cdot}10^{-2}$	$9.13{\cdot}10^{-3}$	$1.61{\cdot}10^{-1}$	113
100	95	105	$2.23{\cdot}10^{-1}$	$6.59{\cdot}10^{-2}$	$8.46{\cdot}10^{-3}$	$2.10{\cdot}10^{-1}$	266
100	100	95	$2.53{\cdot}10^{-1}$	$8.58{\cdot}10^{-2}$	$1.79{\cdot}10^{-3}$	$1.62{\cdot}10^{-1}$	251
100	100	100	$2.38{\cdot}10^{-1}$	$7.77{\cdot}10^{-2}$	$8.81{\cdot}10^{-4}$	$1.21{\cdot}10^{-1}$	271
100	100	105	$2.53{\cdot}10^{-1}$	$8.19{\cdot}10^{-2}$	$3.40{\cdot}10^{-4}$	$7.43{\cdot}10^{-2}$	167
100	105	95	$2.59{\cdot}10^{-1}$	$8.74{\cdot}10^{-2}$	$6.46{\cdot}10^{-3}$	$2.17{\cdot}10^{-1}$	460
100	105	100	$2.36{\cdot}10^{-1}$	$7.28{\cdot}10^{-2}$	$6.65{\cdot}10^{-3}$	$8.53{\cdot}10^{-2}$	471
100	105	105	$2.35{\cdot}10^{-1}$	$7.49{\cdot}10^{-2}$	$5.68{\cdot}10^{-3}$	$8.28{\cdot}10^{-2}$	163
105	95	95	$2.97{\cdot}10^{-1}$	$9.39{\cdot}10^{-2}$	$1.03{\cdot}10^{-2}$	$1.53{\cdot}10^{-1}$	148
105	95	100	$2.66{\cdot}10^{-1}$	$7.71{\cdot}10^{-2}$	$8.67{\cdot}10^{-3}$	$2.89{\cdot}10^{-1}$	251
105	95	105	$2.53{\cdot}10^{-1}$	$7.07{\cdot}10^{-2}$	$8.77{\cdot}10^{-3}$	$1.75{\cdot}10^{-1}$	230
105	100	95	$3.88{\cdot}10^{-1}$	$1.40{\cdot}10^{-1}$	$5.92{\cdot}10^{-4}$	$1.68{\cdot}10^{-1}$	284
105	100	100	$2.66{\cdot}10^{-1}$	$8.15{\cdot}10^{-2}$	$8.84{\cdot}10^{-4}$	$7.89{\cdot}10^{-2}$	313
105	100	105	$2.62{\cdot}10^{-1}$	$7.98{\cdot}10^{-2}$	$6.95{\cdot}10^{-4}$	$6.48{\cdot}10^{-2}$	194
105	105	95	$2.90{\cdot}10^{-1}$	$9.22{\cdot}10^{-2}$	$6.40{\cdot}10^{-3}$	$1.77{\cdot}10^{-1}$	186
105	105	100	$2.75{\cdot}10^{-1}$	$8.78{\cdot}10^{-2}$	$5.92{\cdot}10^{-3}$	$6.01{\cdot}10^{-2}$	115
105	105	105	$2.69{\cdot}10^{-1}$	$8.20{\cdot}10^{-2}$	$6.66{\cdot}10^{-3}$	$1.46{\cdot}10^{-1}$	170

Table 6: Three-layered wall example: summary of results corresponding to the sensitivity analysis with respect to material parameters. Discrepancy measures for each case. Perturbations of ±5% were performed in the material parameter c in the three layers.

objective data can increase up to 42% for the RRD field, 80% for the RSs and 1000% for the displacements (from $8.81 \cdot 10^{-4}$ to $1.03 \cdot 10^{-2}$). These results highlight the importance of the simultaneous identification of RRDs and material parameters and are in line with previous findings [37]. Despite this, Figure 16 shows that it is possible to adequately estimate the RRDs in the media and intima layers when the material parameters are given with errors up to 5% in the parameter characterizing the isotropic response of the material (sensitivity with respect to other material parameters is still to be evaluated). Moreover, it is also noteworthy that in some cases, the introduced errors in the constitutive parameter result in a decrease of the relative discrepancies of the estimated RRDs, RSs and/or displacement fields. This could be explained by the fact that the optimization algorithm seems to be unable to consistently find the global minimum of the functional.

6. Concluding remarks

A variational framework was proposed for the characterization of RRDs in arterial walls. In this process, the load-free configuration of that vessel is also obtained. The proposed approach relies on a cost functional which measures the mechanical imbalance caused by an inconsistent RRD field. Following the idea of the virtual fields method [32], this cost functional is based in the variational formulation of the equilibrium equations. In this case, the mechanical setting is enriched taking into account the action of RRDs and RSs, and the equilibrium equations are presented for the mentioned load-free configuration together with a set of known loaded configurations. Moreover, the proposed cost functional is constructed regardless the number of test functions to evaluate the equilibrium. Then, the RRDs characterization problem is transformed into the minimization problem of such functional.

The examples shown in this work highlight the suitability of this approach, evidencing that the minimization of the proposed functional successfully leads to the characterization of RRDs, yielding encouraging results for the three explored cases.

Observe that the proposed methodology could also be applicable to the estimation of constitutive parameters. While such questions have been increasingly addressed in the literature [35, 42] in the last years (using, however, completely different approaches), the lack of contributions regarding the estimation of RRDs motivated the subject of the present work. Inspired by the sensitivity analysis presented here, and by recent findings reported in the literature, a challenging continuation of this work would be to formulate a strategy to simultaneously characterize these parameters along with the residual deformations.

As a matter of fact, although the proof-of-concept examples discussed are problems with rotational symmetry, it is important to remark that the presented framework has been developed in 3D space with no additional kinematic simplifications. Although the large amount of required input data and the additional technical complexities currently constitute a limitation for its application in patient-specific cases, the proposed strategy proved to be effective

towards the formalization of the RRD identification problem. Moreover, if advances in medical image acquisition systems and motion tracking techniques are able to accurately provide the required data, methodologies based on the ideas exposed in this work could be used to perform the estimation of RRDs in in-vivo settings. For the potential success in such scenarios it will be fundamental to adopt strategies for the interpolation of the objective fields in order to limit the number of unknown parameters. It is also important to note that the proposed method has also shown potential for its direct application in in-vitro settings, offering an alternative for the identification of RRDs via non-destructive experimentation.

Finally, the exploration of more sophisticated optimization algorithms and criteria for the choice of weighting parameters are being matter of current research, as well as the sensitivity of uncertainties in input data, such as equilibrium configurations, pressure loads and displacement fields.

Acknowledgments

This work was partially supported by the Brazilian agencies CNPq and FAPERJ. The support of these agencies is gratefully acknowledged.

Conflict of interest

The authors declare that they have no conflict of interest.

AppendixA. Optimization configuration

For the optimization problems described in the examples detailed in Sections 5.2 and 5.3, we make use of the function *fmincon* available from the MATLAB Optimization Toolbox. For both problems, the following options are set as

- *AlwaysHonorConstraints* set to *none*,
- *GradObj* set to *off*,
- *Hessian* set to *bfgs*,
- *InitTrustRegionRadius* set to 40,
- *TolCon* set to 10^{-12},
- *TolFun* set to 10^{-8},
- *MaxFunEvals* set to 10^6, and
- *MaxIter* set to 10^5,

while remaining parameters are taken by default.

References

[1] G. A. Holzapfel, T. C. Gasser, A new constitutive framework for arterial wall mechanics and a comparative study of material models, J. Elast. 61 (2000) 1–48.

[2] Y. C. Fung, What are the residual stresses doing in our blood vessels?, Ann. Biomed. Eng. 19 (1991) 237–249.

[3] M. A. Zulliger, P. Fridez, K. Hayashi, N. Stergiopulos, A strain energy function for arteries accounting for wall composition and structure, J. Biomech. 37 (2004) 989–1000.

[4] H. Weisbecker, D. M. Pierce, P. Regitnig, G. A. Holzapfel, Layer-specific damage experiments and modeling of human thoracic and abdominal aortas with non-atherosclerotic intimal thickening., J. Mech. Behav. Biomed. 12 (2012) 93–106.

[5] G. A. Holzapfel, R. Ogden, Constitutive modelling of arteries, P Roy. Soc. A-Math. Phy. 466 (2118) (2010) 1551–1597.

[6] Y. C. Fung, S. Q. Liu, Change of residual strains in arteries due to hypertrophy caused by aortic constriction., Circ. Res. 65 (5) (1989) 1340–9.

[7] G. A. Holzapfel, G. Sommer, M. Auer, P. Regitnig, R. W. Ogden, Layer-specific 3D residual deformations of human aortas with non-atherosclerotic intimal thickening., Ann. Biomed. Eng. 35 (4) (2007) 530–45.

[8] P. J. Blanco, G. D. Ares, S. A. Urquiza, R. A. Feijóo, On the effect of preload and pre-stretch on hemodynamic simulations : an integrative approach, Biomech. Model Mechanobiol.

[9] M. L. Raghavan, S. Trivedi, A. Nagaraj, D. D. McPherson, K. B. Chandran, Three-Dimensional Finite Element Analysis of Residual Stress in Arteries, Ann. Biomed. Eng. 32 (2) (2004) 257–263.

[10] J. Ren, Growth and residual stresses of arterial walls., J. Theor. Biol. 337 (2013) 80–8.

[11] I. Hariton, G. DeBotton, T. C. Gasser, G. A. Holzapfel, Stress-driven collagen fiber remodeling in arterial walls, Biomech. Model Mechanobiol. 6 (January) (2007) 163–175.

[12] A. Valentín, J. D. Humphrey, Evaluation of fundamental hypotheses underlying constrained mixture models of arterial growth and remodelling., P Roy. Soc. A-Math. Phy. 367(1902) (2009) 3585–3606.

[13] J. D. Humphrey, K. R. Rajagopal, A constrained mixture model for growth and remodeling of soft tissues, Math. Models Methods Appl. Sci. 12 (2002) 407–430. arXiv:0036013702.

[14] D. Li, A. M. Robertson, A structural multi-mechanism damage model for cerebral arterial tissue., J. Biomech. Eng 131 (10) (2009) 101013.

[15] C. J. Cyron, J. D. Humphrey, Vascular homeostasis and the concept of mechanobiological stability., Int. J Eng. Sci. 85 (2014) 203–223.

[16] K. Takamizawa, K. Hayashi, Strain energy density function and uniform strain hypothesis for arterial mechanics., J. Biomech. 20 (1) (1987) 7–17.

[17] M. Destrade, Y. Liu, J. Murphy, G. Kassab, Uniform transmural strain in pre-stressed arteries occurs at physiological pressure, J Theor Biol.

[18] V. Alastru, A. Gara, E. Pea, J. F. Rodrguez, M. A. Martnez, M. Doblar, Numerical framework for patient-specific computational modelling of vascular tissue, International Journal for Numerical Methods in Biomedical Engineering 26 (1) (2010) 35–51.

[19] D. M. Pierce, T. E. Fastl, B. Rodriguez-Vila, P. Verbrugghe, I. Fourneau, G. Maleux, P. Herijgers, E. J. Gomez, G. A. Holzapfel, A method for incorporating three-dimensional residual stretches/stresses into patient-specific finite element simulations of arteries, Journal of the Mechanical Behavior of Biomedical Materials 47 (2015) 147–164.

[20] L. A. Taber, J. D. Humphrey, Stress-modulated growth, residual stress, and vascular heterogeneity., J. Biomech. Eng.-T ASME 123 (6) (2001) 528–535.

[21] C. Bellini, J. Ferruzzi, S. Roccabianca, E. Di Martino, J. Humphrey, A microstructurally motivated model of arterial wall mechanics with mechanobiological implications, Ann. Biomed. Eng. 42 (3) (2014) 488–502.

[22] J. Schröder, M. von Hoegen, An engineering tool to estimate eigenstresses in three-dimensional patient-specific arteries, Computer Methods in Applied Mechanics and Engineering 306 (2016) 364–381.
[23] M. Gee, C. Reeps, H. Eckstein, W. Wall, Prestressing in finite deformation abdominal aortic aneurysm simulation., Jounal of Biomechanics 42 (2009) 1732–1739.
[24] M. W. Gee, C. Forster, W. A. Wall, A computational strategy for prestressing patient-specific biomechanical problems under finite deformation, International Journal for Numerical Methods in Biomedical Engineering 26 (1) (2010) 52–72.
[25] H. Weisbecker, D. M. Pierce, G. A. Holzapfel, A generalized prestressing algorithm for finite element simulations of preloaded geometries with application to the aorta, Int J Numer Meth Biomed Engng 30 (2014) 857–872.
[26] S. Govindjee, P. A. Mihalic, Computational methods for inverse finite elastostatics, Comput. Meth. Appl. Mech. Eng. 136 (1-2) (1996) 47 – 57.
[27] J. Lu, X. Zhou, M. L. Raghavan, Inverse elastostatic stress analysis in pre-deformed biological structures: Demonstration using abdominal aortic aneurysms, J. Biomech. 40 (40) (2007) 693–696.
[28] L. Speelman, E. M. H. Bosboom, G. W. H. Schurink, J. Buth, M. Breeuwer, M. J. Jacobs, F. N. van de Vosse, Initial stress and nonlinear material behavior in patient-specific AAA wall stress analysis, Journal of Biomechanics 42 (11) (2009) 1713–1719.
[29] X. Zhou, M. L. Raghavan, R. E. HarbRag, J. Lu, Patient-specific wall stress analysis in cerebral aneurysms using inverse shell model, Ann Biomed Eng.
[30] P. Seshaiyer, J. D. Humphrey, A sub-domain inverse finite element characterization of hyperelastic membranes including soft tissues, Journal of biomechanical engineering 125 (3) (2003) 363–371.
[31] J. Stalhand, A. Klarbring, M. Karlsson, Towards in vivo aorta material identification and stress estimation, Biomech. Model Mechanobiol. 2 (2004) 169–186.
[32] M. Grédiac, F. Pierron, S. Avril, E. Toussaint, The virtual fields method for extracting constitutive parameters from full-field measurements: a review, Strain 42 (4) (2006) 233–253.
[33] I. Masson, P. Boutouyrie, S. Laurent, J. D. Humphrey, M. Zidi, Characterization of arterial wall mechanical behavior and stresses from human clinical data, J Biomech 41 (12) (2009) 2618–2627.
[34] S. Avril, P. Badel, A. Duprey, Anisotropic and hyperelastic identification of in vitro human arteries from full-field optical measurements, Journal of Biomechanics 43 (15) (2010) 2978 – 2985.
[35] A. Wittek, K. Karatolios, P. Bihari, T. Schmitz-Rixen, R. Moosdorf, S. Vogt, C. Blase, In vivo determination of elastic properties of the human aorta based on 4D ultrasound data, J. Mech. Behav. Biomed. 27 (2013) 167–183.
[36] E. van Disseldorp, N. Petterson, M. Rutten, F. van de Vosse, M. van Sambeek, R. Lopata, Patient specific wall stress analysis and mechanical characterization of abdominal aortic aneurysms using 4d ultrasound, European Journal of Vascular and Endovascular Surgery (2016) –.
[37] X. Guo, J. Zhu, A. Maehara, D. Monoly, H. Samady, L. Wang, K. L. Billiar, J. Zheng, C. Yang, G. S. Mintz, D. P. Giddens, D. Tang, Quantify patient-specific coronary material property and its impact on stress/strain calculations using in vivo ivus data and 3d fsi models: a pilot study, Biomechanics and Modeling in Mechanobiology (2016) 1–12.
[38] The MathWorks Inc, Matlab optimization toolbox r2013b (2013).
[39] R. H. Byrd, M. E. Hribar, J. Nocedal, An Interior Point Algorithm for Large-Scale Nonlinear Programming, SIAM J. Optimiz. 9 (1999) 877–900.
[40] R. H. Byrd, J. C. Gilbert, J. Nocedal, A trust region method based on interior point techniques for nonlinear programming, Math. Program. 89 (1) (2000) 149.
[41] J. D. Humphrey, Remodeling of a collagenous tissue at fixed lengths., J. Biomech. Eng.-T ASME 121 (1999) 591–597.
[42] L. Bertagna, M. D'Elia, M. Perego, A. Veneziani, Fluid-Structure Interaction and Biomedical Applications, Springer Basel, Basel, 2014, Ch. Data Assimilation in Cardiovascular Fluid–Structure Interaction Problems: An Introduction, pp. 395–481.

HIGHLIGHTS: Identification of residual stresses in multi-layered arterial wall tissues using a variational framework

A novel variational framework for the characterization of residual deformations (and stresses) in arterial walls is proposed.

A cost functional is presented to measure the mechanical imbalance, caused by inconsistent residual stresses, for a set of known equilibrium configurations.

The identification of residual stresses is achieved through the minimization of such cost functional.

Numerical experiments provide evidence of the viability of the proposed methodology.